AGU PUBLICATIONS

Water Resources Research

RESEARCH ARTICLE
10.1002/2016WR019126

Key Points:
- We use time-lapse geophysical data to directly forecast physical property in the subsurface
- We use a prior set of models to establish a linear relationship between data and forecast in a reduced dimension space
- We estimate the full posterior distribution of the physical property with the established linear relationship for observed data

Supporting Information:
- Supporting Information S1

Correspondence to:
T. Hermans,
thermans@stanford.edu or
thomas.hermans@ulg.ac.be

Citation:
Hermans, T., E. Oware, and J. Caers (2016), Direct prediction of spatially and temporally varying physical properties from time-lapse electrical resistance data, *Water Resour. Res.*, *52*, doi:10.1002/2016WR019126.

Received 26 APR 2016
Accepted 5 SEP 2016
Accepted article online 8 SEP 2016
Published online 22 SEP 2016
Corrected 30 SEP 2016

This article was corrected on 30 SEP 2016. See the end of the full text for details.

Direct prediction of spatially and temporally varying physical properties from time-lapse electrical resistance data

Thomas Hermans[1], Erasmus Oware[2], and Jef Caers[1]

[1]Department of Geological Sciences, Stanford University, Stanford, California, USA, [2]Department of Geology, State University of New-York at Buffalo, Buffalo, New York, USA

Abstract Time-lapse applications of electrical methods have grown significantly over the last decade. However, the quantitative interpretation of tomograms in terms of physical properties, such as salinity, temperature or saturation, remains difficult. In many applications, geophysical models are transformed into hydrological models, but this transformation suffers from spatially and temporally varying resolution resulting from the regularization used by the deterministic inversion. In this study, we investigate a prediction-focused approach (PFA) to directly estimate subsurface physical properties with electrical resistance data, circumventing the need for classic tomographic inversions. First, we generate a prior set of resistance data and physical property forecast through hydrogeological and geophysical simulations mimicking the field experiment. We reduce the dimension of both the data and the forecast through principal component analysis in order to keep the most informative part of both sets in a reduced dimension space. Then, we apply canonical correlation analysis to explore the relationship between the data and the forecast in their reduced dimension space. If a linear relationship can be established, the posterior distribution of the forecast can be directly sampled using a Gaussian process regression where the field data scores are the conditioning data. In this paper, we demonstrate PFA for various physical property distributions. We also develop a framework to propagate the estimated noise level in the reduced dimension space. We validate the results by a Monte Carlo study on the posterior distribution and demonstrate that PFA yields accurate uncertainty for the cases studied.

1. Introduction

Over the last few decades, hydrogeophysics has emerged as a new, interdisciplinary, field of sciences that aims at better understanding of hydrological processes through geophysical methods. Geophysical surveys are designed to acquire data related to the subsurface such as subsurface structures (e.g., conceptualization of the aquifer), hydraulic property spatial distributions (such as porosity and hydraulic conductivity) or the monitoring of physical properties of an aquifer (e.g., saturation, salinity or concentration, temperature) [e.g., *Rubin and Hubbard*, 2005; *Vereecken et al*., 2007; *Binley et al*., 2015; *Linde et al*., 2015].

Among the large number of hydrogeophysical methods (for a review, see *Binley et al*. [2015]), the number of time-lapse applications of electrical methods has grown significantly (for a review, see *Singha et al*. [2015]). The electrical resistivity of many fluid bearing sediments and rocks is largely dominated by the volumetric fluid content and the fluid electrical conductivity. Time-lapse electrical methods are therefore particularly well-suited for the monitoring of dynamic processes such as the evolution of saturation in the vadose zone [e.g., *Binley et al*., 2002; *Koestel et al*., 2008], solute transport [e.g., *Doetsch et al*., 2012; *Robert et al*., 2012], heat transport [e.g., *Hermans et al*., 2014; *Arato et al*., 2015], contaminant remediation operations [e.g., *Truex et al*., 2013; *Johnson et al*., 2015; *Masy et al*., 2016] or CO_2 sequestration [e.g., *Carrigan et al*., 2013; *Auken et al*., 2014]. The goal of hydrogeophysics is not just to quantify the change in resistivity caused by those processes, but also to infer the related change in physical properties such as water content and saturation, salinity or temperature. Knowing the spatio-temporal distribution of such physical properties is important for forecasting/managing purposes in water resources, agriculture or geothermal applications. Examples include the need to irrigate when the moisture content is too small, pumping control when salt water intrusion reaches the capture zone of a well, the adaptation of heat injection or extraction if the temperature reaches a given threshold in a geothermal system. In addition, regardless of any application, the

quantification of the physical properties constitutes a major and fundamental area of research within hydrogeophysics to study subsurface dynamics [*Singha et al*., 2015].

The most common strategy is to transform geophysical parameters into physical or hydrologic properties through a petrophysical relationship from field or laboratory measurements [*Singha et al*., 2015]. The geophysical parameters are most often obtained through a deterministic regularized inversion. However, the deterministic regularized approach used to invert geophysical data often yields a smeared distribution of the hydrologic or physical parameters. Indeed, the solution of the geophysical inverse problem is nonunique and results obtained from deterministic inversion sometimes lack geological realism [*Linde et al*., 2015]. Many authors have observed poor recovery of mass-balance in tracing experiments [e.g., *Singha and Gorelick*, 2005; *Müller et al*., 2010] and over- or underestimation of the physical properties due to over-smoothing of the geophysical image [e.g., *Vanderborght et al*., 2005; *Hermans et al*., 2015]. Some authors have proposed alternative constraints to the standard smoothness constraint in order to reduce smoothing and better estimate physical properties [*Doetsch et al*., 2010; *Fiandaca et al*., 2015; *Caterina et al*., 2014; *Nguyen et al*., 2016; *Hermans et al*., 2016], but the inherent limitations of deterministic inversion remain.

One major issue with the classic deterministic inversion is the spatially varying resolution of the inversion method that prevents the direct use of petrophysical relationships at the field scale [*Day-Lewis et al*., 2005] and strongly depends on the regularization operator. To overcome this limitation, *Moysey et al*. [2005] and *Singha and Moysey* [2006] proposed Monte Carlo simulations of numerical analogs of the monitoring experiment to derive a field-scale cell-by-cell petrophysical relationship, within the modeling grid. Similarly, *Oware et al*. [2013] used hydrological analog models to derive, through proper orthogonal decomposition (POD), a physically-based regularization operator able to reproduce physically plausible property distributions. An underlying limitation of deterministic approaches is their lack of proper uncertainty quantification in the distribution of geophysical parameters, despite that the solution is known to be nonunique. *Audebert et al*. [2014] developed a method based on multiple deterministic inversions with various regularization parameters and clustering to better delineate zone(s) affected by resistivity changes; but their uncertainty concerns only the zone affected by resistivity changes and not their amplitude.

The issue of variable resolution also extends to the time dimension. Time-lapse inversion schemes with temporal regularization constraints (4D deterministic inversion) have been developed by *Kim et al*. [2009] and *Karaoulis et al*. [2011]. Even if they generally ensure coherent variations of geophysical parameters with time, they still suffer from the limitation arising from regularization.

Another approach is the use of summary statistics of the physical property (temporal and spatial moments) which may be sufficient to identify advection and dispersion effects [e.g., *Kemna et al*., 2002; *Vanderborght et al*., 2005; *Koestel et al*., 2008]. However, the regularization in the inversion process still influences the estimation of spatial moments [*Day-Lewis et al*., 2007]. The inverse problem may be formulated in terms of plume geometry [*Ben Hadj Miled and Miller*, 2007; *Pidlisecky et al*., 2011; *Laloy et al*., 2012]. In this case, the number of model parameters is reduced by using the first spatial moments of the geophysical parameter distribution, making the inverse problem overdetermined and allowing the efficient use of Markov chain Monte Carlo (McMC) methods [*Laloy et al*., 2012]. However, the limited number of spatial moments used for inversion limits the accuracy of the inverted model in case of complex geological distributions of the physical properties.

The estimated geophysical images or spatial moments, with their inherent limitations, may subsequently be used, possibly with a petrophysical transformation, to calibrate a hydrogeological model [e.g., *Binley et al*., 2002; *Briggs et al*., 2013]. The modeler may account for the resolution limitations of tomograms by adequately weighting the geophysics-derived information [*Hermans et al*., 2012] in order to limit the influence of imperfect estimates of physical quantities in the calibration process. For example, filtering schemes have been proposed to account for the varying resolution of tomograms [*Caterina et al*., 2013] and applied in hydrogeophysical inversion [*Beaujean et al*., 2014].

An alternative approach is to seek correlation in time between geophysical and hydrological data. Time series and spectral analysis can provide quantitative information on dynamic processes occurring in aquifers [*Johnson et al*., 2012; *Wallin et al*., 2013]. However, the method still suffers from the same limitations regarding the inversion itself, such as variable resolution and lack of (hydro)geological realism.

Finally, coupled inversion approaches have gained popularity in the last few years [e.g., *Hinnell et al*., 2010; *Irving and Singha*, 2010]. In this procedure, geophysical data are directly included in the hydrologic inversion process, suppressing the need for a geophysical inversion and postinversion petrophysical transform. The hydrologic model output is used as input for geophysical forward modeling through a petrophysical relationship and the corresponding geophysical response is compared to the observed data. Coupled inversion approaches are efficient when only a few hydrologic parameters are calibrated but might be difficult to apply in complex and heterogeneous cases [*Christensen et al*., 2016], because it strongly depends on the hydrological conceptual model itself and its inherent assumptions (boundary conditions, prior). The method also becomes computationally demanding when used within a stochastic framework to quantify uncertainty [*Irving and Singha*, 2010].

In this paper, we propose a prediction-focused approach (PFA) [e.g., *Satija and Caers*, 2015; *Scheidt et al*., 2015] to forecast the spatio-temporal change in physical properties using the changes in resistance collected during time-lapse electrical resistivity tomography (ERT), without explicitly inverting for the resistivity distribution. Note that in this paper we keep the terminology "forecast" used in previous studies even if the physical property is not estimated in the future but simultaneously to the data. Similarly to *Moysey et al*. [2005] and *Oware et al*. [2013], we use analog or prior models to simulate the hydrogeophysical experiment. The use of aquifer analogs ensures geological realism in the approach, which is essential to produce physically-plausible results [*Linde et al*., 2015]. However, instead of using a regularization-based framework, we aim to directly derive the full posterior distribution of physical properties from time-lapse ERT, without any iterative inversion. To achieve this, we establish a direct multivariate statistical model between the data variables (changes in resistance) and the forecast variables (variations in physical property) in the section where data were collected. We then use the statistical model to establish a full posterior uncertainty quantification of the forecast given the actual observed data. Although our method is Bayesian, it differs from previous Bayesian methods developed in hydrogeophysics and hydrogeology [e.g., *Rubin et al*., 2010; *Murakami et al*., 2010, *Chen et al*., 2012; *Linde et al*., 2015]. In PFA, the likelihood is computed in a reduced dimension statistical framework. Moreover, the likelihood is not formulated based on the model parameters but based on the target (physical) variables. PFA directly builds a joint bivariate distribution between data and forecast (target variables) in reduced dimension space. From the joint distribution, posterior distribution of forecast given data can then be readily sampled, without additional forward model evaluations or inversion.

Satija and Caers [2015] applied the PFA to forecast the contamination in a pumping well from concentration measurements upstream from this well, i.e., data and forecast were punctual time series of the same property. They showed that PFA yields results similar to the rejection sampler. In this work, we extend the PFA to the use of geophysical data to forecast subsurface physical properties. We also demonstrate that the method is successful to forecast complex spatio-temporal series. A topic not covered by *Satija and Caers* [2015] is the propagation of noise through PFA. This issue is an important concern for geophysical data sets. We propose a specific framework based on Monte Carlo simulations to prevent erroneous estimates due to not accounting for the proper noise propagation. With several case examples, we demonstrate the robustness, methodological and computational simplicity of the approach.

2. Methods

2.1. Overview of the Methodology

The principle of the PFA is to directly estimate the posterior distribution of the physical property $\boldsymbol{h}$ of interest $f_H(\boldsymbol{h}|\boldsymbol{d_{obs}})$ without explicitly transforming the observed geophysical data $\boldsymbol{d_{obs}}$ into a distribution of geophysical parameters. We therefore avoid inverting the time-lapse geophysical data sets and using a petrophysical transform *after* inversion that can be space-dependent and uncertain [*Singha et al*., 2015]. The key of the PFA is to work in a reduced dimension space to establish a statistical model between geophysical data and physical properties to be able to estimate the full posterior distribution of the forecast for some observed data. The PFA developed for this specific case involves six steps:

1. generation of prior sets of data and forecast, sampled from the prior distribution,
2. dimension reduction of the data and forecast variables using principal component analysis,
3. canonical correlation analysis to establish a multivariate correlation between data and forecast variables,

4. Gaussian process regression (kriging) with the observed data to derive the conditional mean and covariance matrix of the forecast variables (in the canonical component space),
5. sampling the Gaussian model,
6. back-transform of the samples into the original high-dimension space.

Steps 1–3 correspond to the training stage, where the relationship between data and forecast in the reduced dimension space is learned from forward simulations on the prior set of models. Steps 4–6 correspond to the forecast stage, where the full posterior distribution of the prediction is deduced from the observed data.

2.2. Generating a Prior Set of Models

Establishing a statistical model between data and forecast requires knowing both for some known subsurface realizations. A realization is the distribution of subsurface parameters required to simulate data and forecast. We generate a prior set of n realizations of the subsurface $\boldsymbol{m}$, here through geostatistical modeling, and simulate (equation (1)) the model response $\boldsymbol{h}$ corresponding to the monitored process, here subsurface flow and transport

$$\boldsymbol{h}=g_H(\boldsymbol{m}) \tag{1}$$

where g_H is the physics-based forward model operator. The model response $\boldsymbol{h}$ is generally the evolution of a given physical property at l different locations at t different time-steps in the subsurface. In the prior set, $\boldsymbol{h}$ is therefore a high dimension array of n realizations of $l \times t$ variables and constitutes the prior distribution of the forecast.

Then, for each realization of this prior, the corresponding geophysical data $\boldsymbol{d}$ are computed using a geophysical forward model g_D

$$\boldsymbol{d}=g_D(\boldsymbol{h},\boldsymbol{m}) \tag{2}$$

For ERT, the data are changes in resistance at t different time steps (subtraction with the background) for u different electrode configurations. In the prior set, $\boldsymbol{d}$ is therefore an array of n realizations of $u \times t$ variables, also high dimensional.

Since $\boldsymbol{h}$ is a physical property and not a geophysical parameter, a petrophysical relationship linking both is used in g_D. In time-lapse studies, the relations between the change of physical properties and geophysical parameters are relatively well-known and more straightforward than in static studies [*Linde et al*., 2015]. The petrophysical relationship can vary depending on the values of $\boldsymbol{m}$, which is therefore a parameter of equation (2). Note that the PFA in general remains valid if data and forecast are not colocated and not simultaneous (the dimension t can be different for data and forecast), i.e. the methodology can be applied to a broader range of problems than time-lapse geophysical inversion [*Satija and Caers*, 2015].

2.3. Dimension Reduction of the Data and Forecast Using Principal Component Analysis

Principal component analysis (PCA) is a multivariate analysis technique that aims at transforming a set of observed variables into a set of linearly uncorrelated variables, called principal components [*Krzanowski*, 2000]. Typically, the first k components of the PCA decomposition, with $k \ll n$, explain almost all the variance of the data set. By keeping only those k first dimensions, one thus achieves an efficient dimension reduction. PCA is based on the eigen-decomposition of a matrix and has been applied on training images by *Oware et al*. [2013] to derive a physically-based operator for the inversion of ERT data. The method is also at the basis of truncated singular value decomposition which is widely applied to regularize underdetermined inverse problems as those encountered in hydrogeology [e.g., *Tonkin and Doherty*, 2005].

We first apply independently PCA on both the data and forecast variables to reduce their dimension to p and q, respectively. The reduced data and forecast variables after PCA are denoted by $\boldsymbol{d}^f$ ($p \times 1$) and $\boldsymbol{h}^f$ ($q \times 1$).

2.4. Linearization Using Canonical Correlation Analysis Between Data and Forecast

The relationship between $\boldsymbol{d}^f$ and $\boldsymbol{h}^f$ is often nonlinear, due to the petrophysical relationships and underlying partial differential equations. Canonical correlation analysis (CCA) is a multivariate analysis method that can be used to transform the relationships between pairs of vector variables with n replicates into a set of

independent linearized relationships between pairs of scalar [*Krzanowski*, 2000]. Mathematically, CCA finds the coefficients in $\boldsymbol{a_i}$ ($p \times 1$) and $\boldsymbol{b_i}$ ($q \times 1$) with $i=1 \ldots m$ that maximize the correlation between the linear combinations $\boldsymbol{a_i^T d^f}$ and $\boldsymbol{b_i^T h^f}$. The resulting linear combinations are denoted by $\boldsymbol{d_i^c}$ and $\boldsymbol{h_i^c}$, and called the canonical variates of $\boldsymbol{d^f}$ and $\boldsymbol{h^f}$. The coefficient of correlation between their n scalar values is called the canonical correlation. The vectors $\boldsymbol{a_i}$ ($p \times 1$) and $\boldsymbol{b_i}$ ($q \times 1$) are orthogonal to each other. The maximum number of canonical variate pairs m that can be found is the minimum of the ranks of $\boldsymbol{d^f}$ and $\boldsymbol{h^f}$. Since p and q are generally much smaller than n, m corresponds to the minimum of p and q. The canonical transformation yields two reduced data variables $\boldsymbol{d^c}$ and $\boldsymbol{h^c}$, such that

$$\boldsymbol{d^c} = \boldsymbol{d^f A^T} \tag{3}$$

$$\boldsymbol{h^c} = \boldsymbol{h^f B^T} \tag{4}$$

with $\boldsymbol{A} = [\boldsymbol{a}_1 \ \ldots \ \boldsymbol{a_m}]$ and $\boldsymbol{B} = [\boldsymbol{b}_1 \ \ldots \ \boldsymbol{b_m}]$.

The canonical transformation can be found through the eigen-decomposition of the sample covariance matrix [*Krzanowski*, 2000]. If $p > q$, i.e. more dimensions are kept in the data, this transformation is reversible

$$\boldsymbol{h^f} = \boldsymbol{B}^{-1} \boldsymbol{h^{cT}}, \tag{5}$$

This back transformation to the original space is essential for the last step of the process.

2.5. Gaussian Process Regression

We use Bayes' rule in formulating the problem of estimating the posterior distribution of $\boldsymbol{h}$ for some observed data $\boldsymbol{d_{obs}}$

$$f_H(\boldsymbol{h}|\boldsymbol{d_{obs}}) = k f_H(\boldsymbol{h}) L(\boldsymbol{h}|\boldsymbol{d_{obs}}) \tag{6}$$

where $f_H(\boldsymbol{h})$ is the prior distribution, $L(\boldsymbol{h}|\boldsymbol{d_{obs}})$ is a likelihood function and k is a proportionality constant. PCA and CCA enable reducing a set of high-dimensional variables ($\boldsymbol{d}$,$\boldsymbol{h}$) to another set of much reduced dimension variables($\boldsymbol{d^c}$, $\boldsymbol{h^c}$), linearly related and whose axes are orthogonal. By back transformation of $\boldsymbol{h^c}$ in the original space (equation (5)), the forecasting problem (equation (6)) is tantamount to forecasting $\boldsymbol{h^c}$ from $\boldsymbol{d^c_{obs}}$. Our goal is thus to obtain the posterior distribution

$$f_H(\boldsymbol{h^c}|\boldsymbol{d^c_{obs}}) = k f_H(\boldsymbol{h^c}) L(\boldsymbol{h^c}|\boldsymbol{d^c_{obs}}) \tag{7}$$

If the canonical correlation of the first components of those reduced dimension variables is large enough, i.e., that a linear relationship between the respective components of $\boldsymbol{d^c}$ and $\boldsymbol{h^c}$ exists, then a Gaussian process regression can be used to solve the problem of estimating $\boldsymbol{h^c}$ from $\boldsymbol{d^c_{obs}}$ [*Tarantola*, 2005].

The framework described by *Tarantola* [2005] assumes a multivariate Gaussian prior distribution of $\boldsymbol{h^c}$, with the mean $\bar{\boldsymbol{h}}^{\boldsymbol{c}}$ and covariance $\boldsymbol{C_{Hc}}$ estimated from the sample distribution. If the marginal distributions of $\boldsymbol{h^c}$ are not Gaussian, then a histogram transform needs to be performed. We now model the relationship between $\boldsymbol{d^c}$ and $\boldsymbol{h^c}$ through the linear forward model operator $\boldsymbol{G}$

$$\boldsymbol{d^c} = \boldsymbol{G h^c} \tag{8}$$

Because the data $\boldsymbol{d_{obs}}$ may be contaminated with noise, its reduced dimension transform $\boldsymbol{d^c_{obs}}$ has observational error $\boldsymbol{C_c^d}$. We will see in the next section how we can model $\boldsymbol{C_c^d}$. The likelihood (in equation (7)) is assumed to be multivariate Gaussian

$$L(\boldsymbol{h^c}|\boldsymbol{d_{obs}}) = \exp\left(-\frac{1}{2}\left(\boldsymbol{G h^c} - \boldsymbol{d^c_{obs}}\right)^T \boldsymbol{C_c^{d-1}} \left(\boldsymbol{G h^c} - \boldsymbol{d^c_{obs}}\right)\right) \tag{9}$$

hence, the posterior distribution is also multivariate Gaussian. The conditional mean and covariance have the following analytical expressions:

$$\tilde{\boldsymbol{h}}_{\boldsymbol{c}} = \left(\boldsymbol{G^T C_c^{d-1} G} + \boldsymbol{C_{Hc}^{-1}}\right)^{-1} \left(\boldsymbol{G^T C_c^{d-1} d^c_{obs}} + \boldsymbol{C_{Hc}^{-1}} \bar{\boldsymbol{h}}^{\boldsymbol{c}}\right) \tag{10}$$

$$\widetilde{C_H^c} = G^T C_c^{d-1} A + C_{Hc}^{-1} \tag{11}$$

Similarly to *Hansen et al*. [2014] and *Satija and Caers* [2015], we use a multivariate Gaussian error model obtained from the residual error in the linear regression (equation (8)) for the prior set to account for the nonperfectly linear relationship between $\boldsymbol{d^c}$ and $\boldsymbol{h^c}$ generally observed for complex systems. The solution in (10) and (11) is modified by adding the covariance term of the error model $\boldsymbol{C_T}$ to the data observational error $\boldsymbol{C_c^d}$, and the mean error $\bar{\epsilon}$ to $\boldsymbol{d_{obs}^c}$. We refer to *Satija and Caers* [2015] for a detailed description of the Gaussian error model.

An obvious advantage of the methodology is that a Gaussian distribution is uniquely defined by its mean and covariance (equations (10) and (11)), and that sampling a Gaussian distribution is straightforward. It is therefore simple to generate s samples $\{\boldsymbol{h_1^c}, \boldsymbol{h_2^c}, \ldots, \boldsymbol{h_s^c}\}$ of the posterior distribution $f_H(\boldsymbol{h^c}|\boldsymbol{d_{obs}})$, each sample being composed of q components. By back transformation of CCA (equation (5)), the q components of $\boldsymbol{h^f}$ are retrieved for the s samples. Then, those q components (first q principal components) are used to estimate s samples of the original high-dimension physical property $\boldsymbol{h}$, by multiplying the reduced components by the inverse matrix of the eigenvectors of the PCA decomposition. Since the vectors are orthonormal, the inverse matrix is equal to its transpose. Those s samples are then used to estimate the statistical properties of the posterior distribution $f_H(\boldsymbol{h}|\boldsymbol{d_{obs}})$.

2.6. Noise Correlation in PCA Space

Solving equations (10) and (11) requires the definition of the covariance matrix of observational error in the canonical space $\boldsymbol{C_c^d}$. The canonical space is related to the principal component space through linear relationships (equation (3)), and therefore $\boldsymbol{C_c^d}$ is linearly related to the error covariance in principal component space $\boldsymbol{C_f^d}$ through

$$\boldsymbol{C_c^d} = \boldsymbol{A}\boldsymbol{C_f^d}\boldsymbol{A^T} \tag{12}$$

The error covariance in the principal component space expresses the error that is made on the estimation of the principal component scores due to the noise on the data. If we express the observed data $\boldsymbol{d_{obs}}$ as a function of the true data $\boldsymbol{d_{true}}$ corrupted by some noise perturbation ϵ

$$\boldsymbol{d_{obs}} = \boldsymbol{d_{true}} + \epsilon \tag{13}$$

the error on the estimation of principal components can be similarly expressed as

$$\epsilon^{\boldsymbol{f}} = \boldsymbol{d_{obs}^f} - \boldsymbol{d_{true}^f} \tag{14}$$

However, the noise observed in the data cannot be easily transformed in the principal component space. Indeed, the different electrode configurations are affected to various degrees by the noise, depending on the strength of the measured signal. The variable transformation in PCA will also affect differently the principal components which have decreasing variance contributions and are affected differently by noise. Hence obtaining some analytical expression for $\boldsymbol{C_f^d}$ is unfeasible. We here propose to use Monte Carlo experiments to estimate the effect of noise in the principal and canonical component space:

1. we use established methods to estimate an error model ϵ (equation (13)), such as reciprocal measurements in electrical methods [*LaBrecque et al*., 1996; *Flores Orozco et al*., 2012];
2. for the *first* of the n samples of the prior set, we replace the noise free data set by noisy data, with a level of noise ϵ (equation (13));
3. we perform PCA on the prior set with the *first* sample contaminated by noise;
4. we compare the principal components of the *first* sample for noisy and noise free data set to deduce $\epsilon_1^{\boldsymbol{f}}$ (equation (14));
5. we repeat Step 2–4 for all other $n-1$ samples of the prior set;
6. we use the obtained set of errors in principal component space $\{\epsilon_1^{\boldsymbol{f}}\ \epsilon_2^{\boldsymbol{f}} \ldots\ \epsilon_{\boldsymbol{n}}^{\boldsymbol{f}}\}$ to estimate $\boldsymbol{C_f^d}$;
7. we estimate $\boldsymbol{C_c^d}$ (equation (12)).

The estimated covariance matrix in the canonical space can now be used in equations (10) and (11) to solve the Gaussian process regression.

3. Applications

In this section, we demonstrate the ability of PFA in a multi time-steps example simulating a heat tracer experiment. We will test the robustness of the method for noisy data and various distributions of the reference forecast. For all examples, from n realizations (see equations (1) and (2)), we choose one as the reference solution and the corresponding data as the actual observed data $\boldsymbol{d}_{obs}$. We forecast the posterior distribution after which we can compare the results with the reference solution.

A comparison between PFA and POD [*Oware et al*., 2013] is presented in the supporting information Text S1 and Figure S1).

3.1. Multi Time-Steps Thermal Tracer Experiment

The methodology is applied here for forecasting a heat tracer experiment. The heat tracer experiment mimics the injection of heated water ($\Delta T = 40°C$) into a confined alluvial aquifer for 24 h at a rate of 3 m^3/h. The tracer flows in the aquifer under forced gradient conditions, induced by pumping at 30 m^3/h in a well located at 20 m from the injection. At 8 m from the injection well, centered on the direction linking injection and pumping well, a cross-borehole ERT plot is considered. The distance between the two boreholes is 4.5 m (Figure 1a). The boreholes are equipped with 13 electrodes spaced every 50 cm from 0.5 to 6.5 m deep, covering the alluvial deposits (Figure 1b).

3.2. Prior Set

The alluvial deposits are represented by two facies: sand lenses (30%) in a gravel (70%) background. The sand lenses are represented by ellipsoids elongated in the direction of flow with a maximum length of 5 m, a maximum width of 3 m, and a thickness of 2 m. The SNESIM algorithm [*Strebelle*, 2002] is used to simulate 500 unconditional realizations of the aquifer deposits on a 40 $\times$ 60 $\times$ 14 grid with dimensions 1 m $\times$ 1 m $\times$ 0.5 m.

For each realization, the heat injection and transport are simulated with HydroGeoSphere [*Therrien et al*., 2010] using transient, fully-saturated flow. The model was extended 20 m in each direction to reduce the effect of boundary conditions on the flow. The boundary conditions are imposed head mimicking a small natural gradient from the injection to the pumping well and constant temperatures. Flow and transport parameters are considered constant, i.e. the variability in the prior is only related to spatial variability in the distributions of the facies. Only the hydraulic conductivity depends on the facies, it is constant and equal to 10^{-4} and 5×10^{-2} m/s for sand and gravel, respectively.

The forecasted property $\boldsymbol{h}$ is composed of the variations of temperature in the ERT plot at 20 time-steps (every 6 h during 5 days), simulated by the flow and transport model. We use the standard relationship between temperature and water electrical conductivity [*Campbell et al*., 1948] to derive the corresponding change in electrical conductivity.

$$\frac{\sigma_T}{\sigma_{25}} = m_f(T-25)+1 \tag{15}$$

where σ_T is the water electrical conductivity at temperature T (in °C) and m_f is the fractional change of conductivity by °C. We use $m_f = 0.02°C^{-1}$ in accordance with values found in the literature [e.g., *Hermans et al*., 2014] and $\sigma_{25} = 0.04$ S/m. Both can be easily measured on a water sample. The background resistivity of

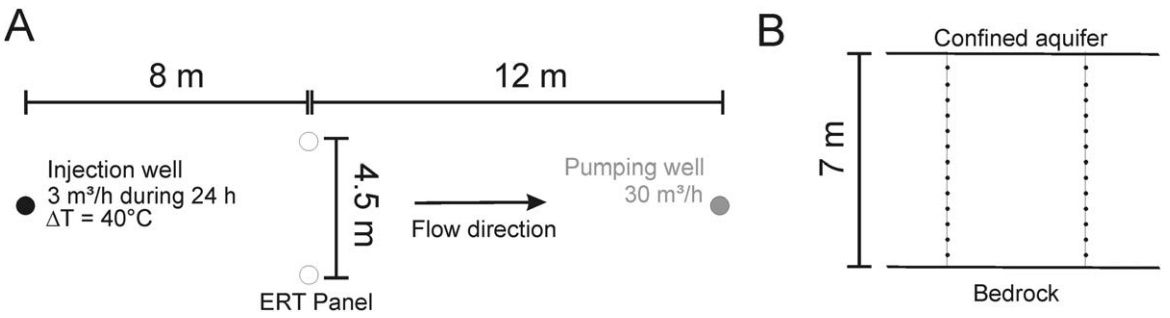

Figure 1. (a) Experimental set-up of the heat tracing test. (b) Electrode location in the ERT plot.

sand and gravel are respectively 160 and 120 Ohm.m and we used the ratio of Archie's law between two time-steps to link the change in water and bulk electrical conductivity. This allows expressing the temperature-dependence of electrical conductivity without defining the formation factor [*Hermans et al.*, 2014].

Based on these resistivity distributions, an ERT resistance data set is simulated for each time step with a combination of AB-MN and AM-BN bipole-bipole configurations [*Zhou and Greenhalgh*, 2000]. The total number of resistance data is 1436. Finally, we compute the change in resistance by subtracting at each time step the resistance corresponding to the background resistivity. This constitutes our data set $\boldsymbol{d}$.

3.3. Posterior Distribution of the Temperature Change From Noise-Free Data

The choice of the dimensions q and p to retain in PCA is driven by the represented variance [e.g., *Oware and Moysey*, 2014]. The dimension q kept for the forecast must therefore represent enough variance to propose realistic samples of the physical property. For low dimension forecasts such as a time series at a given location, explaining more than 99% of the variance is feasible [*Satija and Caers*, 2015]. However, for high dimension forecasts such as those considered here with two spatial dimensions and one temporal dimension, a lower cut-off is expected.

Part of the data may be uninformative about the forecast, hence it is not always necessary to retain 99% or more of the variance of the data to choose the dimension p. However, we generally observe an increase in correlation coefficients in CCA when more dimensions are kept in the data. To ensure the back transform of CCA, p has also to be higher than q. As will be shown in the next section, the choice of the dimension should rather be dictated by considerations on the noise level and kept to a level sufficiently low compared to the number of models in the prior set.

The noise free data are composed of 20 series of 1436 resistance changes, i.e., a total of 28,720 dimensions for each of the 500 realizations. However, resistance data exhibit a very high level of redundancy and 90% of the spatiotemporal variance is represented by the first 3 principal components, 99% by the first 12 components and 99.95% by the first 50 dimensions. In this example, we keep the first 50 dimensions in the data in a reduced data set $\boldsymbol{d}^{\boldsymbol{f}}$.

The forecast is composed of the value of temperature changes at the 28 $\times$ 26 cells (25 cm $\times$ 25 cm) of the grid used for forward ERT modeling, giving a total of 14560 dimensions for the 499 different realizations of the prior set (the reference forecast is not considered). 90% of the variance is explained by the first 8 principal components, 95% by the first 14 and 99% by the first 35 dimensions. We keep the first 14 dimensions in the reduced forecast $\boldsymbol{h}^{\boldsymbol{f}}$. This ensures a reliable spatio-temporal reconstruction of the forecast with a relatively low number of dimensions.

CCA is applied on the reduced data sets in order to maximize the correlation between the components of the data and forecast variables (Figure 2). In this case, the proposed dimension reduction is efficient: the correlation coefficient for the four first dimensions, carrying most of the variance, is above 0.99. For higher dimensions, a linear relationship is still observed until dimension 14, supporting the use of the Gaussian regression.

We generate 300 samples of the posterior distribution $f_H\left(\boldsymbol{h}^{\boldsymbol{c}}|\boldsymbol{d}^{\boldsymbol{c}}_{\boldsymbol{obs}}\right)$ which were subsequently back transformed to the physical space. Four samples of the distribution are shown with the reference solution at 4 selected time steps in Figure 3. The samples successfully identify the temporal behavior of the temperature distribution as well as the location and relative spread of temperature changes. Most differences between samples are related to the value of the maximum change in temperature. Almost all samples show an abrupt decrease in temperature at 6 m depth, as observed in the reference solution.

The spatial and temporal characteristics of the posterior distribution are summarized in Figure 4. The spatiotemporal mean of the samples slightly overestimates the maximum change in temperature but clearly identifies the zone affected by a change in temperature. The standard deviation shows that most variability is related to the time-step exhibiting maximum change (i.e., t = 36 h). The maximum value of the standard deviation is observed at the location of the abrupt temperature decrease, which shows that it is a region difficult to resolve. Figure 4b shows the mean temperature in the plot at the different time steps for the prior, the posterior and the reference distributions. This illustrates that the ERT data are very efficient in reducing uncertainty on the mean temperature in the plot compared to the prior distribution. The PFA also clearly

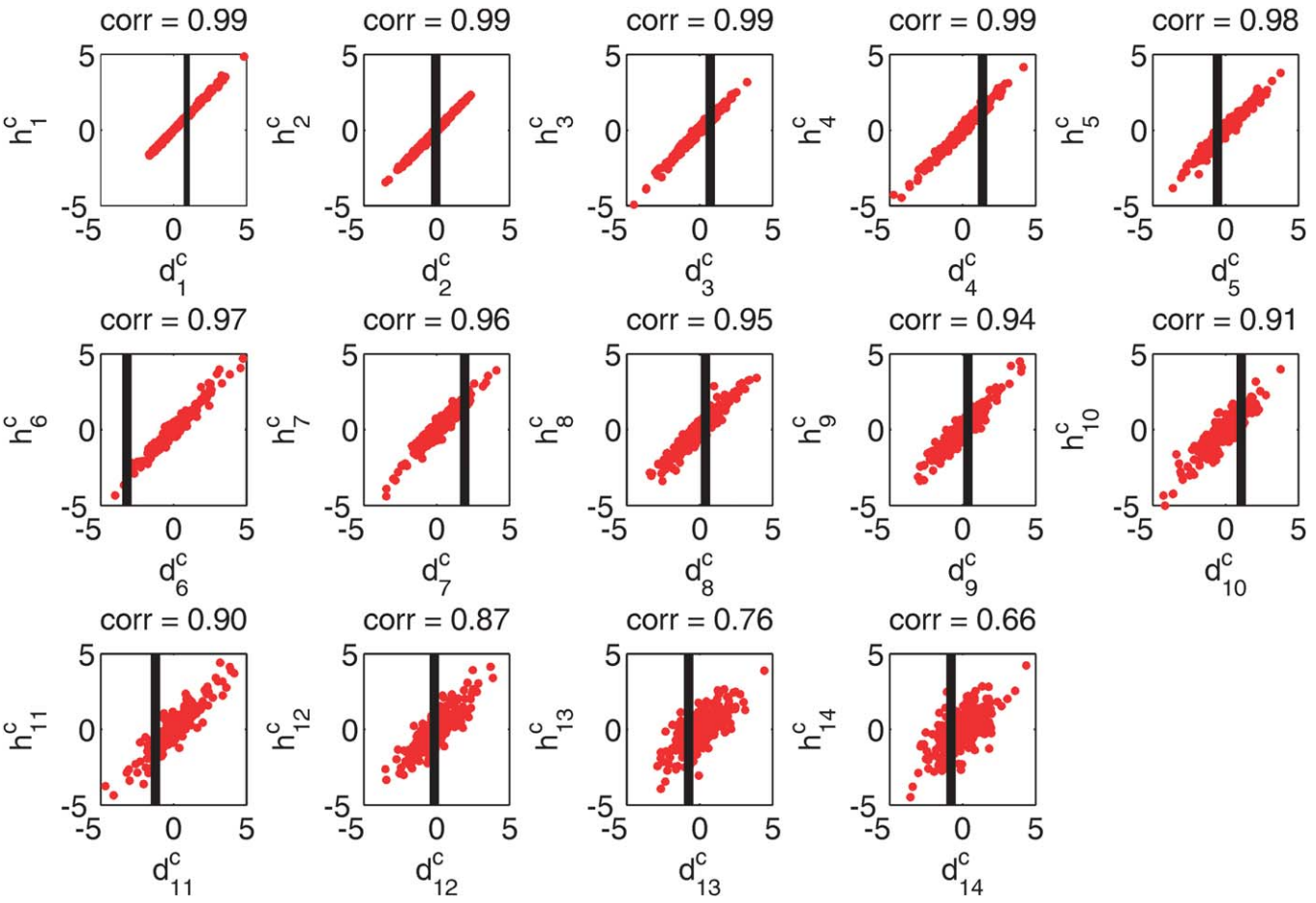

Figure 2. Canonical correlation analysis of the principal components of the change in resistance data (50 dimensions) and change in temperature (14 dimensions). A linear relation is clearly visible with correlation coefficient above 0.9 for the first eleven components. The black lines show the position of the observed data.

identifies the temporal behavior of the tracer, because the maximum change in temperature is not observed at the same time step for the reference as for most of the models in the prior set (36 h instead of 30 h).

3.4. Posterior Distribution of the Temperature Change From Noisy Data

We perform Monte Carlo simulations with noisy data to evaluate how the noise is propagated into the PCA component scores. Figure 5 shows the estimated covariance matrix for 2 different cases. The first case corresponds to a 1% random Gaussian noise added to the changes in resistance. The error thus increases with the change in resistance

If the error on the measured resistance is composed of systematic and random components, the first component is cancelled out when using data difference, but the random component can be additive. If the actual resistance between two-time steps does not change, but that the random component does, the resulting error for a zero change in resistance can be as high as for a larger change in resistance.

The second case therefore considers a level of noise independent of the change in resistance. The error distribution is symmetric around a zero mean with a 0.034 Ohm standard deviation, the proportion of large errors decreases exponentially: 50% of the absolute errors are below 0.004 Ohm and 90% below 0.0483 Ohm. The histogram of the error distribution is presented in the supporting information Figure S2. The median absolute change in resistance for the whole data set is 0.018 Ohm; therefore, the ratio of the median absolute error on the median absolute resistance change is 22%. The median of the relative error distribution is 18%. The overall error level is thus much larger than in the first case

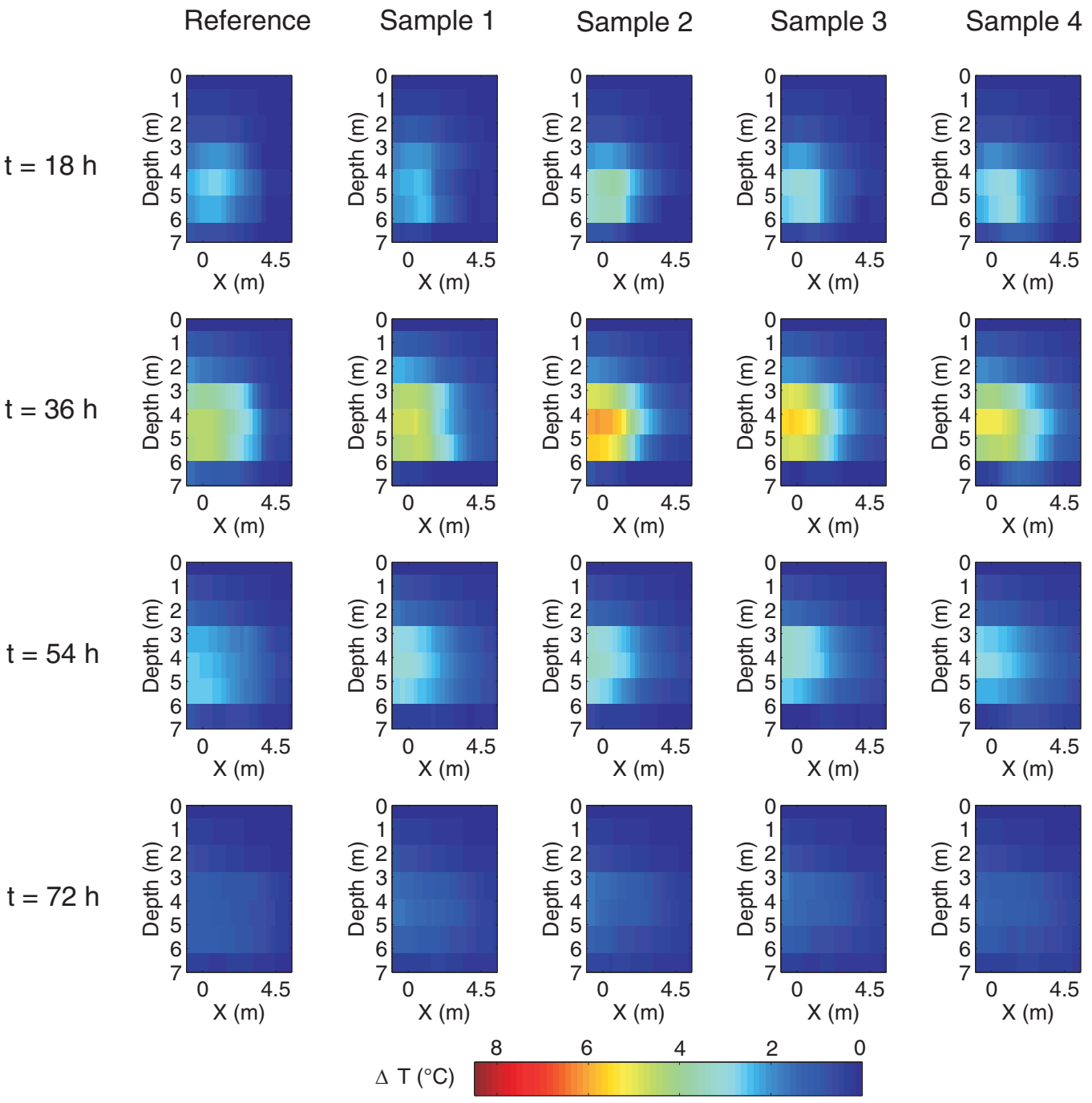

Figure 3. Reference model and four samples of the posterior at four different time steps. The samples correctly catch the spatial and temporal behavior of the temperature distribution. Most variations between samples are related to the amplitude of the maximum temperature.

An illustration of the corresponding noisy data is given in the supporting information Figure S2. The latter case will be referenced as "Independent noise" in the next sections. It is important to note that the proposed methodology can accommodate any noise description or any noise model as it does not rely on any specific assumption concerning the noise distribution. An additional case, with a 10% random Gaussian noise added to the changes in resistance is presented in the supporting information Figures S3 and S4. The interpretation of this case is relatively similar to the "Independent noise" below.

For the 1% Gaussian noise case (first column of Figure 5), the PCA error covariance matrix $\mathbf{C}_{\mathbf{f}}^{\mathbf{d}}$ is sparse, with only a few nonzero entries along the diagonal. The low level of noise has little effect on the estimation of

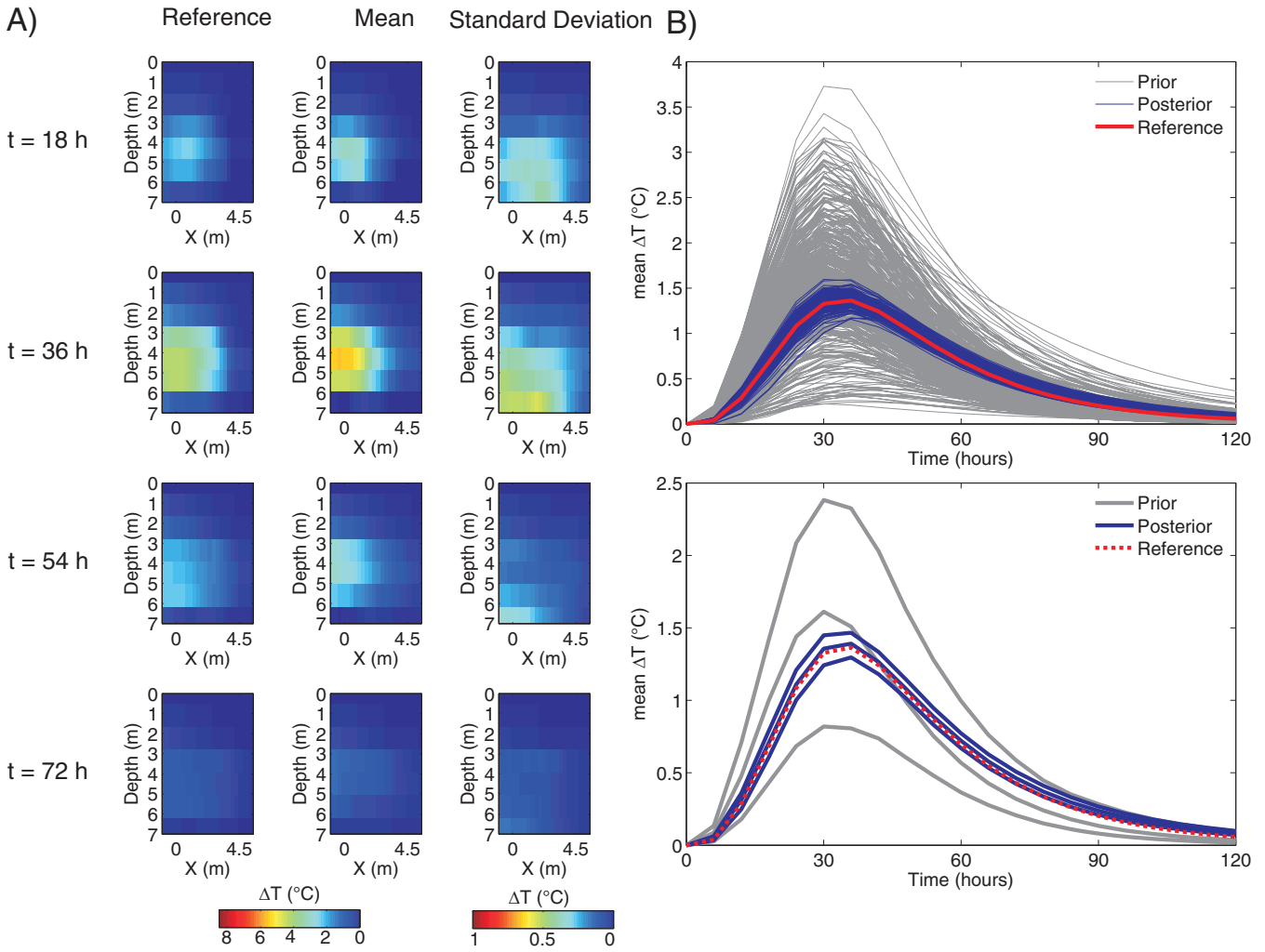

Figure 4. (a) Reference model, mean and standard deviation of the posterior distribution at different time steps. The mean solution slightly overestimates the maximum temperature but the reference solution lies within the posterior. The standard deviation amplitude is higher at the location and time of the maximum temperature change. (b) (top) The posterior distribution of the mean temperature in the plot is displayed with the prior and reference distribution, showing that the proposed solution is a very good estimator of the mean temperature in the plot. (bottom) 10, 50 and 90% quantiles of the distribution.

PCA scores in the first 50 dimensions. The CCA error covariance matrix $\mathbf{C}_c^d$ is computed through equation (12) and shows values close to 0, smaller than the values observed in the error model covariance matrix $\mathbf{C}_T$ whose entries increase with the dimensions, as the correlation decreases. This means that the noise has a negligible effect compared to the error made in the linear regression. The 1% Gaussian noise does not influence the posterior distribution in this case. For the "Independent noise" (second column of Figure 5), the entries of $\mathbf{C}_f^d$ are significantly larger (note the change in the color scale), meaning that the error made on the estimated PCA scores is no longer negligible. $\mathbf{C}_c^d$ entries are one order of magnitude above $\mathbf{C}_T$. Note that $\mathbf{C}_T$ is the same as in the first case (only the color scale is different), as it only depends on the error in the regression model and thus on the number of dimensions used in CCA. An inappropriate estimation of $\mathbf{C}_c^d$ may lead to a poor estimation of the posterior. Note that the estimated $\mathbf{C}_f^d$ is almost a diagonal matrix, which is expected since the principal components are orthogonal and thus uncorrelated.

The analysis of $\mathbf{C}_f^d$ clearly shows that all components are not affected in the same fashion by the noise. In the "Independent noise" case, except for the fourth dimension, the ten first components are well estimated. The error on the PCA scores is particularly high between dimensions 25–40. One possibility is therefore to reduce the number of dimensions in the data set. For example, keeping the 25 first dimensions in the data (third column in Figure 5) still explains 99.7% of the variance and drastically reduces the values of $\mathbf{C}_c^d$. Since less dimensions are used, the linear regression is weaker and the components of $\mathbf{C}_T$ are slightly higher

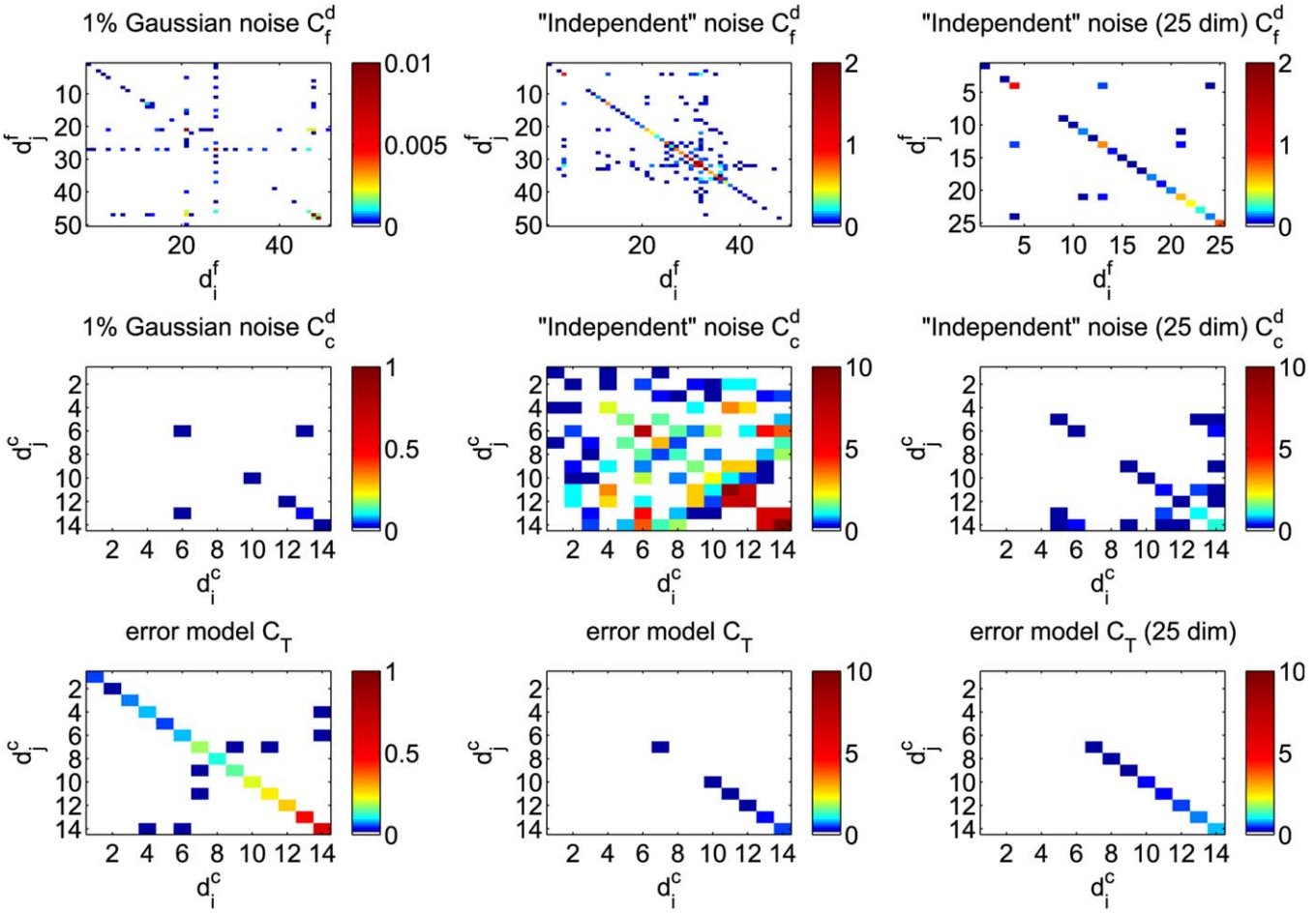

Figure 5. Error covariance matrix in (top) PCA space, (middle row) CCA space and (bottom) Gaussian regression error model covariance matrix for Monte Carlo simulations with change in resistance data contaminated by (left) 1% random Gaussian noise, (middle column) "Independent noise" and (left column) "Independent noise" with only the first 25 dimensions considered.

than when 50 dimensions are kept, such that $\mathbf{C}_c^d$ is of the same order of magnitude as $\mathbf{C}_T$, but only higher dimensions are affected.

The effects of the choice of the data dimensions and the estimation of the error covariance matrix are illustrated in Figures 6 and 7 with the mean and standard deviation of the spatial temperature change for noisy data sets ("Independent noise"). It appears that ignoring the covariance matrix for noisy data when 50 dimensions are used (second column in Figures 6 and 7) yields results contaminated by strong artifacts. The mean of the posterior distribution misses the spatial patterns and shows no temporal coherence. Due to noise, the poor estimation of the CCA scores leads to an unacceptable estimation of the forecast. This stresses the importance of estimating the noise level, as it is the case for standard tomographic inversion. Using the appropriate estimation of $\mathbf{C}_c^d$ (third column) stabilizes the PFA with a mean solution correctly estimating the spatial and temporal trends but with a higher standard deviation compared to the noise free case (first column), as expected.

Using only 25 dimensions in the data enables reducing the impact of noise (fourth and fifth columns). Both solutions with and without estimation of $\mathbf{C}_c^d$ render results similar to the noise free case. Given that less dimensions are used, $\mathbf{C}_T$ has larger values which tends to increase the standard deviation of the posterior. Taking into account the error covariance matrix has little effect on both mean and standard deviations, as the poorly estimated dimensions are not considered in CCA.

The proposed noise propagation procedure identifies clearly the risk for the prediction to be affected by artifacts related to the noise on the data. By analyzing the error covariance matrix in PCA scores, the components affected by the noise are easily identified. They can be disregarded or properly processed by using

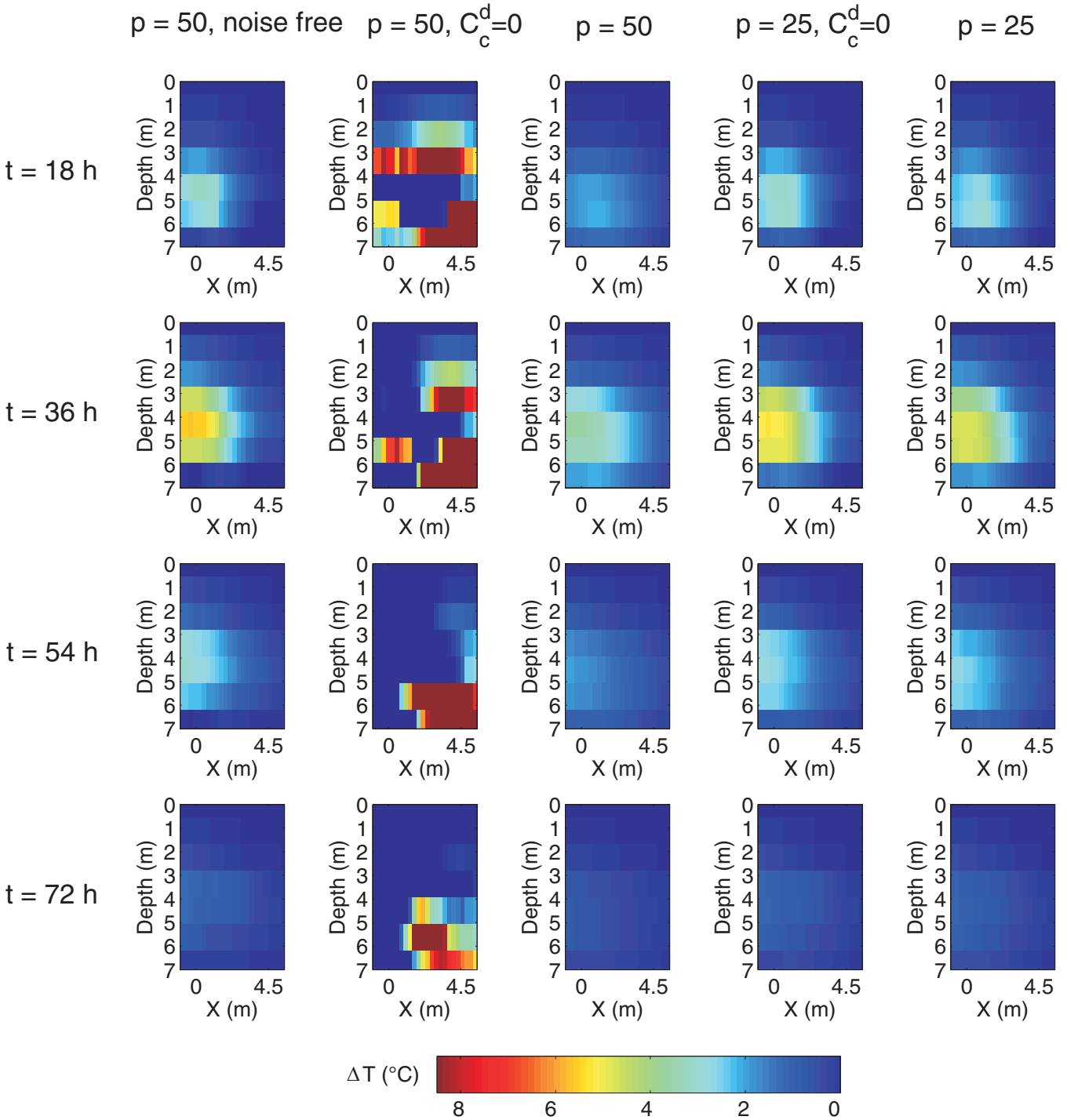

Figure 6. Mean of the posterior distribution at four different time steps for various cases: 50 dimensions in the data and noise free data (column 1), 50 dimensions in the data, noisy data but C_c^d=0 (column 2), 50 dimensions in the data, noisy data and C_c^d estimated with Monte Carlo simulations (column 3), 25 dimensions in the data, noisy data but C_c^d=0 (column 4), 25 dimensions in the data, noisy data and C_c^d estimated with Monte Carlo simulations (column 5).

the covariance matrix for prediction. In this specific case, the conservative choice is to reduce the dimensions of data variables. Indeed, the noise introduced when a high number of dimensions is used is counterbalanced by an estimated covariance matrix with larger components, due to the higher error made on the estimation of PCA scores. This leads to a higher uncertainty on the temperature estimate.

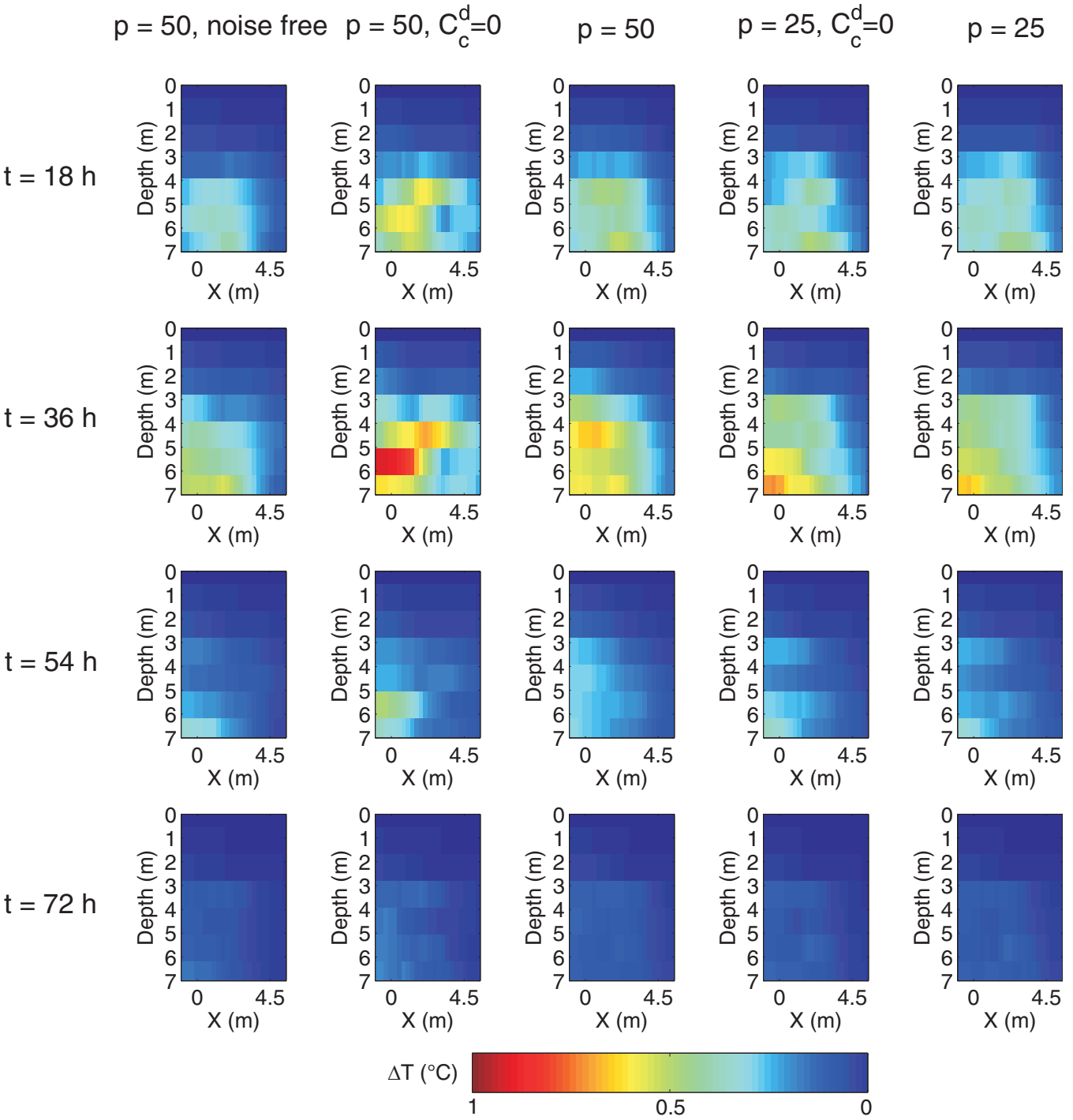

Figure 7. Standard deviation of the posterior distribution at four different time steps for various cases: 50 dimensions in the data and noise free data (column 1), 50 dimensions in the data, noisy data but $C_c^d = 0$ (column 2), 50 dimensions in the data, noisy data and C_c^d estimated with Monte Carlo simulations (column 3), 25 dimensions in the data, noisy data but $C_c^d = 0$ (column 4), 25 dimensions in the data, noisy data and C_c^d estimated with Monte Carlo simulations (column 5).

3.5. Applications to High and Low Temperature References

As shown in Figure 4b, the prior distribution spans a broad range of maximum mean change in temperature, from 0.5 up to 3.5°C. In the previous application, the reference lies in the middle of the prior distribution of the forecast, and therefore many realizations in the prior set are relatively similar to the reference. In this section, we apply the PFA to forecast the temperature for reference realizations at the extreme ends of

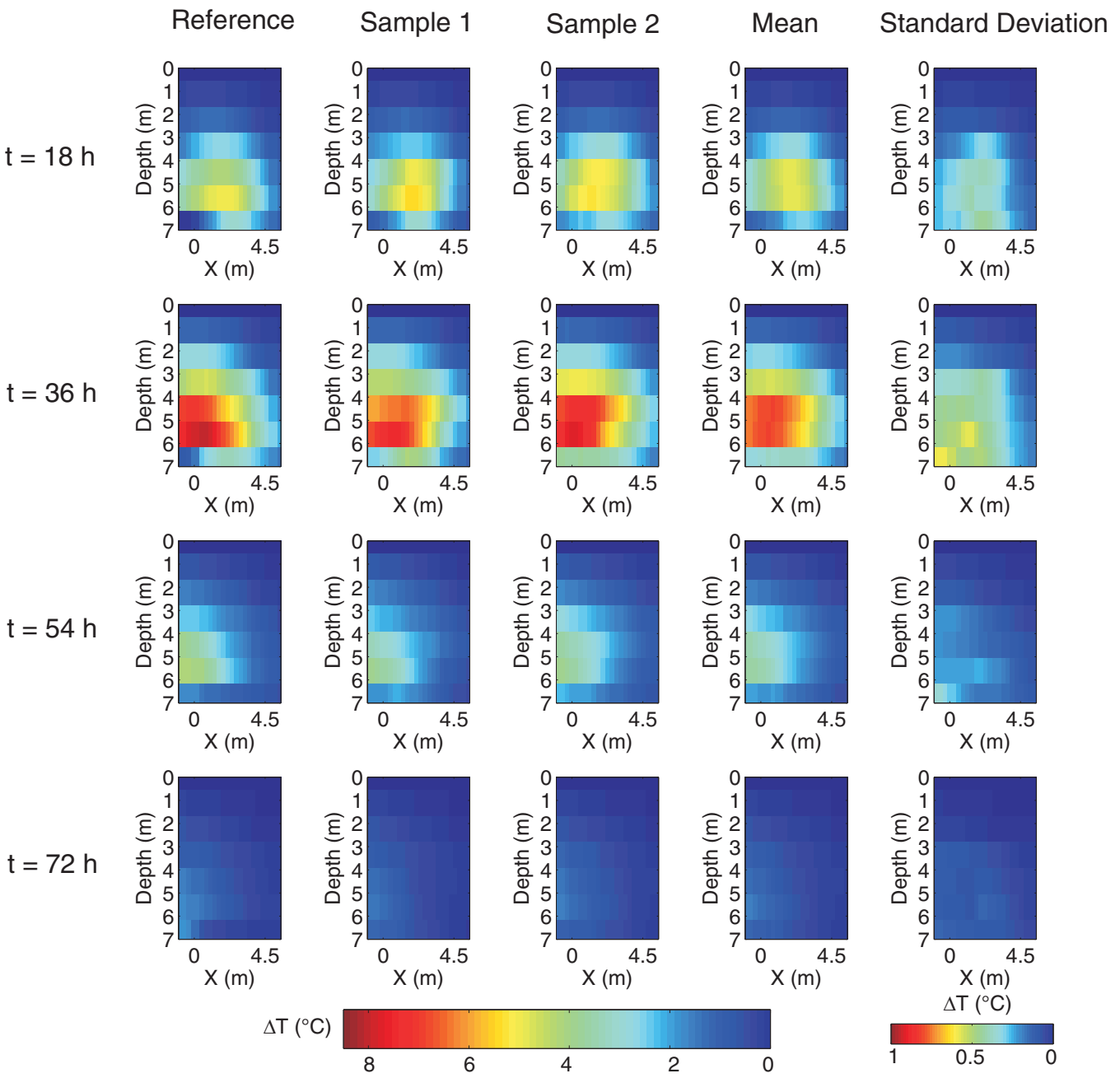

Figure 8. Reference model for a high maximum temperature change (column 1), 2 samples of the posterior (columns 2 and 3), mean and standard deviation of the posterior distribution (columns 4 and 5).

the prior distribution of the forecast with relatively high and low temperature changes respectively. The data correspond to the "Independent noise" case (see section 3.4) and we use the 25 first PCA components of the data variables.

For a high maximum temperature change (Figures 8 and 10), the zone affected by temperature changes, its spreading and its maximum amplitude are correctly identified by the samples of the posterior distributions and the mean. The temporal behavior is also coherent with the reference solution. We observe somewhat more variations in the posterior distribution (higher standard deviation) which are related to the higher amplitude of the anomaly.

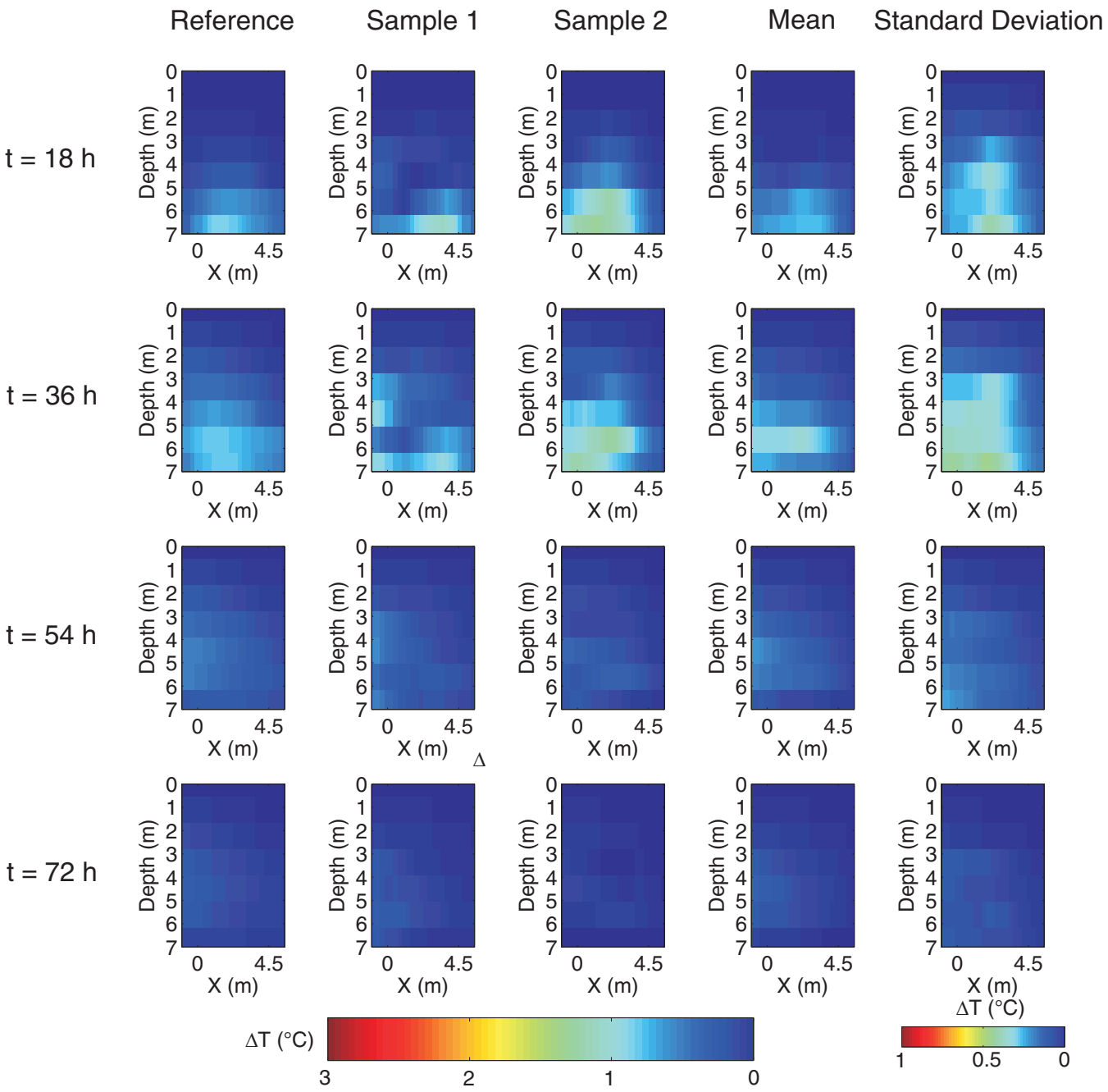

Figure 9. Reference model for a low maximum temperature change (column 1), 2 samples of the posterior (columns 2 and 3), mean and standard deviation of the posterior distribution (columns 4 and 5).

The low temperature change is more difficult to image (Figures 9 and 10). Indeed, low variations in temperature yield low change in resistance so that the measured signal is low. The case displayed in Figure 9 has a maximum change in temperature of 1°C. In addition, it shows a relatively early arrival of the tracer. A change of 1°C corresponds to a change in resistivity of only about 2%, which is often considered as not interpretable in field-scale time-lapse ERT [e.g., *Robert et al*., 2012; *Doetsch et al*., 2012; *Chrétien et al*., 2014; *Hermans et al*., 2012, 2015].

The two displayed samples identify the early arrival, with a maximum temperature slightly higher than the reference. Since some samples of the posterior also display lower maximum temperature changes, the

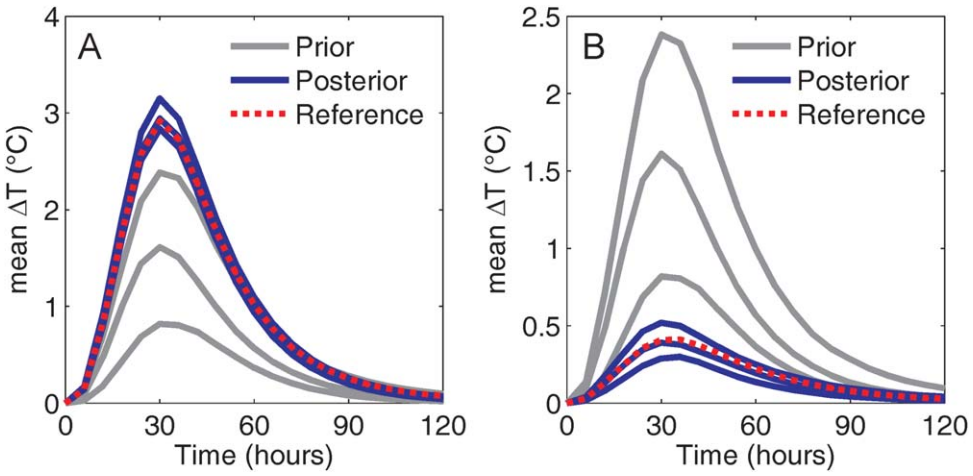

Figure 10. Posterior distribution (10, 50, and 90% quantiles) of the mean temperature in the plot with the prior and reference distribution for (a) the high and (b) low temperature models.

mean solution is relatively close to the reference. The location of the anomaly is correctly imaged. Given the low temperature change, the uncertainty in the posterior is higher than for the two first examples, showing that many temperature distributions can be coherent with the data.

Figure 10 shows the mean temperature in the plot at the different time steps for the prior, the posterior and the reference distributions for the cases illustrated in Figures 8 and 9. In both cases, the reference lies within the posterior distribution whose distributions are much narrower than the prior. This illustrates that the use of ERT data is very efficient in reducing uncertainty related to the mean temperature in the plot, even though the "hot" and "cold" references are above the 90% quantile and below the 10% quantile of the prior distribution, respectively. ERT data also allow the temporal behavior of the tracer to be clearly identified.

For the high temperature case, the reference response is between quantiles 10% and 50% of the posterior. Because many samples are generated between the 10% and 50% quantiles, these two quantiles are very close. This can be related to the small number of realizations sampled in the high temperature region of the prior distribution of the forecast by the prior set (the reference is actually above the 98% quantile of the prior distribution).

For the low temperature case, noisy data may produce small decrease in temperature ($\Delta T < 0$), limited to a few tenth of degrees for some of the samples. This is an indirect effect of the Gaussian regression where values of $\boldsymbol{h}^{\boldsymbol{c}}$ are sampled that are not observed in the data. The PFA is not worse than classical inversions, since similar behaviors are observed in standard inversions showing positive resistivity changes even if only negative changes are expected. It highlights the fact that sampling the forecast in the tail of a distribution is challenging and might require additional models in the prior set.

4. Validation

In this section, we validate the posterior distribution of the forecasted physical properties. *Satija and Caers* [2015] and *Scheidt et al*. [2015] validated their direct forecasting methodology in a hydrogeological context with rejection sampling. Here, we propose, as an alternative, to validate the PFA through a Monte Carlo experiment. In a second step, we verify that the sampled posterior distributions are consistent with the geophysical data.

4.1. Monte Carlo Experiments

The objective of the Monte Carlo experiments is to show that the posterior distributions obtained for many references integrate to the prior distribution. This will show that PFA is an appropriate method to sample the posterior distribution.

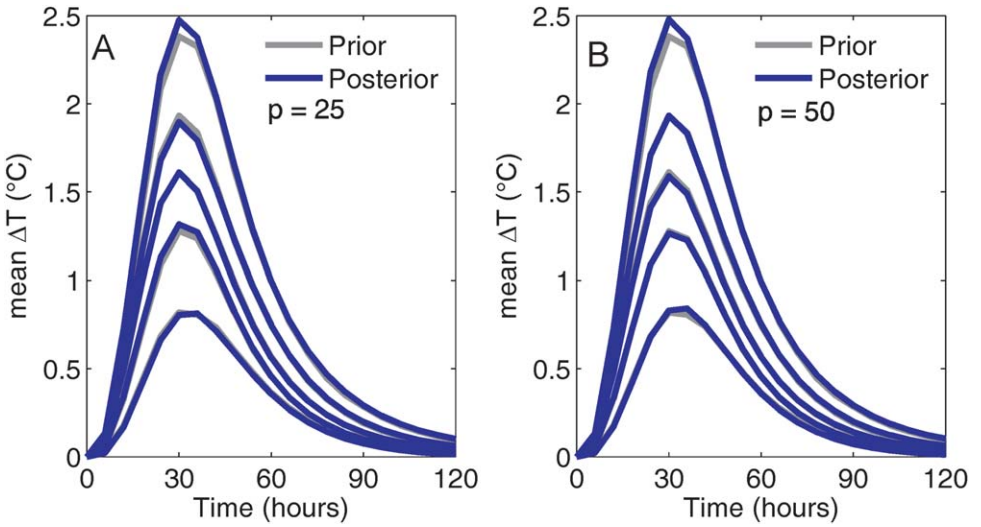

Figure 11. The integral of posterior distribution of the temperature in the ERT plot is compared to the prior distribution using the 10, 25, 50, 75, and 90% quantiles, for (a) 25 dimensions and (b) 50 dimensions in the data. The distributions are almost exactly similar.

Equation (6) expresses the general form of the posterior distribution given the prior distribution and a likelihood function. If we generate Monte Carlo samples to explore the entire data space by subsequently using every sample of the prior set as observed data $\boldsymbol{d}_{obs}$, and integrate the posterior distributions of the forecast we have:

$$\int f_H(\boldsymbol{h}|\boldsymbol{d}) f_D(\boldsymbol{d}) d\boldsymbol{d} = \int \frac{L(\boldsymbol{h}|\boldsymbol{d})}{f_D(\boldsymbol{d})} f_H(\boldsymbol{h}) f_D(\boldsymbol{d}) d\boldsymbol{d} \tag{16}$$

where $f_D(\boldsymbol{d})$ is the prior distribution of the data. The prior distribution of the forecast is independent of $\boldsymbol{d}$

$$\int f_H(\boldsymbol{h}|\boldsymbol{d}) f_D(\boldsymbol{d}) d\boldsymbol{d} = f_H(\boldsymbol{h}) \int L(\boldsymbol{h}|\boldsymbol{d}) d\boldsymbol{d} \tag{17}$$

and the integral of the likelihood over the data space is equal to 1 so that we obtain

$$\int f_H(\boldsymbol{h}|\boldsymbol{d}) f_D(\boldsymbol{d}) d\boldsymbol{d} = f_H(\boldsymbol{h}) \tag{18}$$

Equation (18) states that integrating the s samples of the posterior for the n realizations of the prior set should give a distribution equal to the prior distribution of the forecast. This offers a way to validate that the PFA yields physically plausible samples and to study its validity regarding the number of dimensions kept in the CCA. If equation (18) is not verified, one should question the number of principal components in the data and forecast used in the CCA.

This Monte Carlo validation is illustrated in Figure 11 for 25 and 50 dimensions kept in the data and 14 in the forecast. The curves correspond to some of the quantiles of the prior and integrated posterior distribution. In both cases, the integrated posterior distributions are almost exactly similar to the prior distribution.

4.2. Consistency of the Sampled Posterior of Forecast With Data

Our methodology is defined statistically in a reduced dimension space, such that the Gaussian regression process (or linear inversion) implies that the sampled $\boldsymbol{h}^{\boldsymbol{c}}$ are coherent with the observed reduced data $\boldsymbol{d}^{\boldsymbol{c}}_{obs}$. Therefore an objective function (deterministic inversion) or a likelihood based on the actual observed geophysical data, is not required. There is also no need for any regularization or to run a forward simulation at any step of the PFA, except to build the prior set. In fact, the entire procedure can be perfectly parallelized in terms of the forward modeling.

Nevertheless, we verify the consistency of the sampled posterior with the actual geophysical data [e.g., *Lochbühler et al.*, 2014]. However, since the solution is expressed in terms of physical property (temperature)

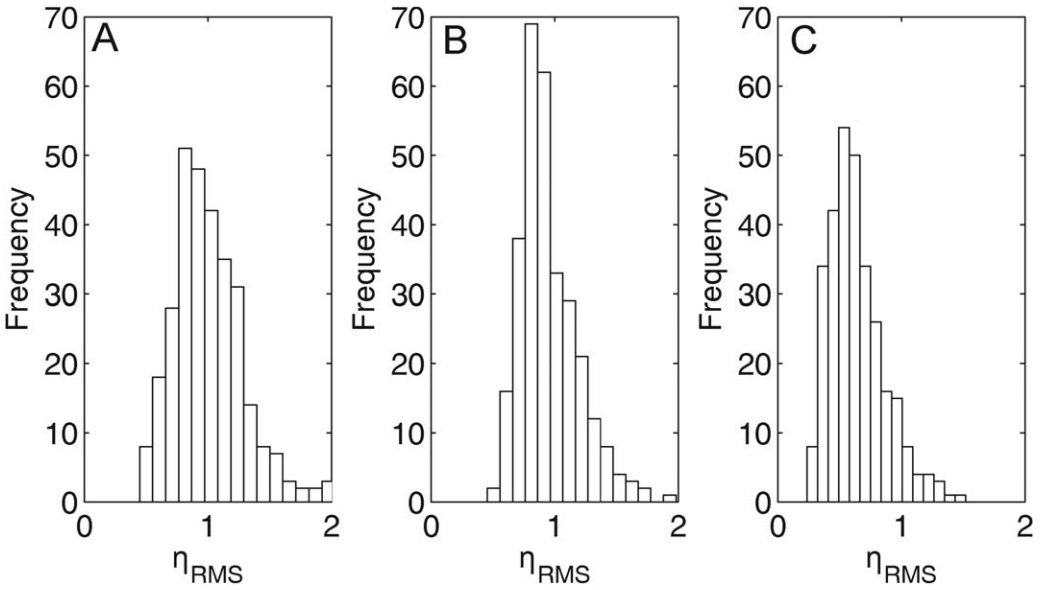

Figure 12. Normalized RMS value of the samples of the posterior distribution for (a) the reference model with intermediate temperature of Figures 6, (b) high temperature of Figure 8 and (c) low temperature of Figure 9. The observed values are within the range of samples fitted to their noise level in standard inversion.

and not resistivity and that the data are expressed in terms of change in resistance, there is no direct way to perform this validation. To overcome this issue, we use the following workflow:

1. the resistances of the background data set are deterministically inverted to obtain a distribution of resistivity $\boldsymbol{\rho_{BG}}$, we do not use the true resistivity because they would be unknown in practice;
2. through the petrophysical relationship used for the creation of the prior set (equation (15)), we transform, for each time step, the change in temperature $\boldsymbol{\Delta T}$ into a change in resistivity $\boldsymbol{\Delta\rho}$ that we add to $\boldsymbol{\rho_{BG}}$ to get $\boldsymbol{\rho_{TL}}$; note that there is no issue of resolution-dependent petrophysical relationship, since no constraint on the model was imposed to derive $\boldsymbol{\Delta T}$;
3. we compute the resistances for each time step and deduce the data, i.e. the changes in resistance $\boldsymbol{\Delta R_{calc}} = \boldsymbol{d_{calc}}$;
4. we calculate the data misfit between $\boldsymbol{d_{true}}$, the noise free reference data set, and $\boldsymbol{d_{calc}}$ through the root-mean-square error (RMS) normalized by the value of RMS between noise free and noisy data

$$\eta_{RMS} = \frac{\sqrt{\sum_i^{ut} \left(\boldsymbol{d_{calc,i}} - \boldsymbol{d_{true,i}}\right)^2}}{\sqrt{\sum_i^{ut} \left(\boldsymbol{d_{obs,i}} - \boldsymbol{d_{true,i}}\right)^2}} \tag{19}$$

   where u is the number of resistance data and t the number of time steps in the monitoring process;

5. we repeat Steps 2–4 for the s samples of the posterior.

The above workflow was applied to the samples of the posterior distribution corresponding to the 3 reference realizations, i.e., intermediate, high and low mean temperature changes, shown respectively in Figures 6, 8 and 9 with 25 dimensions kept in the data and the "Independent noise" level. The posterior consists of 300 samples and the histogram of their normalized error η_{RMS} is shown in Figure 12. For the three cases, the mode of the histogram is around 1, i.e., an error corresponding to the noise level in the data. This shows that the proposed methodology is able to generate realistic distribution of the physical properties of interest in accordance with geophysical data, without explicitly running the geophysical forward operator during the inversion process.

5. Conclusions

We propose to solve the estimation of physical properties with geophysical data with a direct forecast approach, the PFA, as an alternative to existing deterministic inversions broadly used in geophysics. The PFA enables directly estimating the spatio-temporal posterior distribution of physical properties, such as

salinity or temperature, to be directly sampled from geophysical time-series. The method is based on generating a prior set of models mimicking the experiment of interest. After dimension reduction of the data and forecast with principal component analysis and canonical correlation analysis, we use a Gaussian regression in the reduced dimension space to sample the posterior distribution. Then, the samples in the reduced space are back transformed to the original space.

We applied the PFA in a heat tracer experiment for a broad range of amplitude variations. The methodology is able to correctly identify the spatio-temporal behavior of the tracer, as well as the amplitude of the maximum change. The spatio-temporal distribution of temperature is complex. We retained 14 dimensions explaining 95% of the variance. It signifies that small-scale features of the forecast corresponding to higher dimensions cannot be reproduced by the method. The corresponding loss of resolution can be assessed by applying this dimension reduction on models from the prior set.

We proposed to analyze the propagation of noise in the reduced component space through Monte Carlo simulations to estimate the error covariance matrix in the reduced dimension space. This step is necessary to stabilize the inversion and shows that reducing the number of dimension in the data can drastically increase the robustness of the method regarding noise.

We validated the approach by verifying the consistency of the samples of the posterior distribution with the geophysical data and the prior distribution. However, the geophysical parameters are never explicitly inverted in the PFA.

In contrast to hydrogeophysical modeling using standard regularized geophysical inversion techniques, the method is (i) stochastic, i.e., the solution is composed of samples of the full posterior distribution and not a single deterministic solution; (ii) it solves the spatio-temporal physical property distribution and not the geophysical parameter; (iii) it does not require the definition of a regularization term which is recognized to be the major element preventing quantitative integration of geophysical data in hydrogeological models. Using physically-based simulations to build the prior set of model, PFA yields physically plausible forecasts. The key point is to build a prior set in accordance with the expected response.

The major advantage of the methodology is to avoid any regularization procedure required in deterministic inversions. The solutions therefore do not suffer from any spatial bias, spatially and temporally varying resolution or uncertainty in the postinversion petrophysical transformation. Petrophysics is only required to build the prior set. After this step, there is no need to run any forward hydrogeological or geophysical simulation. Therefore, the PFA enables to quickly generate the full posterior distribution of the problem compared to classic stochastic inversion methods. This remains true for problems with a large number of parameters, as long as it is possible to efficiently reduce their dimensions.

Except for building the prior set, the PFA does not require a flow and transport model to generate the posterior distribution. It is thus more flexible than coupled inversion schemes and much faster than stochastic McMC methods. It is therefore a good alternative when only monitoring results are needed or to improve sequential inversion scheme with a physically plausible distribution of the physical property, integrating uncertainty of the estimate.

Nevertheless, the method is limited by the choice of prior parameters involved in the construction of the prior set itself, i.e., on the underlying hydrogeological model and the petrophysical relationship. Indeed, a satisfactory solution will be found only if the actual data lie in the empirical prior distribution of the prior set. Therefore, the method should not be used for extrapolation. If the observed data lie outside of the prior distribution, it signifies that the data are not consistent with the prior. However, this is a limitation for all Bayesian methods, since the Bayesian model requires for the prior to capture data to avoid prior-data inconsistency. PFA has the advantage over other techniques to clearly identify such inconsistency using the joint distribution in the reduced dimension space. Observed data corresponding to extremes of the data prior distribution might be difficult to forecast. In such a case, it might be necessary to generate more realizations in the vicinity of the observed data and therefore increase the number of models in the prior set. Similarly, more models might be needed for prior considering more uncertain parameters such as geological scenarios, boundary conditions or continuous hydraulic conductivity distributions. However, the computational cost of the method would remain lower than stochastic McMC methods.

Extending the distribution of prior parameters in the prior set to allow uncertainty on sensitive parameters such as the petrophysical relationships, the hydraulic conductivity of the deposits and the heterogeneity would

ensure a larger data prior distribution and therefore allow an application of the prior set to a broader range of observed data. Although physically based flow and transport simulations were used to generate the prior set in this study, the PFA applied to geophysical data could also work with a prior set generated differently (e.g., with a geostatistical tool). Creating the prior set would be faster but at the expense of geological realism. The proposed developments will be investigated in future work and tested on a real-world case study.

Acknowledgments
The code and data sets used in this work can be obtained on demand. Please contact the corresponding author. This work was performed by T. Hermans while being the recipient of a fellowship from the Belgian American Educational Foundation for postdoctoral studies at Stanford University. We also thank Wallonia-Brussels International and the Vocatio Foundation for the financial support of T. Hermans during his postdoctoral research stay at Stanford University. We are grateful to E. Huber and F. Nguyen for their careful readings and suggestions. We thank the Associate Editor, Andrew Binley, and 4 anonymous reviewers for their constructive comments.

References

Arato, A., J. Boaga, C. Comina, M. De Seta, E. Di Sipio, A. Galgaro, N. Giordano, and G. Mandrone (2015), Geophysical monitoring for shallow geothermal applications—Two Italian case histories, *First Break*, *33*(8), 75–79.

Audebert, M., R. Clément, N. Touze-Foltz, T. Günther, S. Moreau, and C. Duquennoi (2014), Time-lapse ERT interpretation methodology for leachate injection monitoring based on multiple inversions and a clustering strategy (MICS), *J. Appl. Geophys.*, *111*, 320–333, doi:10.1016/j.jappgeo.2014.09.024.

Auken, E., J. Doetsch, G. Fiandaca, A. V. Christiansen, A. Gazoty, A. G. Cahill, and R. Jakobsen (2014), Imaging subsurface migration of dissolved CO2 in a shallow aquifer using 3-D time-lapse electrical resistivity tomography, *J. Appl. Geophys.*, *101*, 31–41, doi:10.1016/j.jappgeo.2013.11.011.

Beaujean, J., F. Nguyen, A. Kemna, A. Antonsson, and P. Engesgaard (2014), Calibration of seawater intrusion models: Inverse parameter estimation using surface electrical resistivity tomography and borehole data, *Water Resour. Res.*, *50*, 6828–6849, doi:10.1002/2013WR014020.

Ben Hadj Miled, M. K., and E. L. Miller (2007), A projection-based level-set approach to enhance conductivity anomaly reconstruction in electrical resistance tomography, *Inverse Probl.*, *23*(6), 2375–2400, doi:10.1088/0266-5611/23/6/007.

Binley, A., P. Winship, L. J. West, M. Pokar, and R. Middleton (2002), Seasonal variation of moisture content in unsaturated sandstone inferred from borehole radar and resistivity profiles, *J. Hydrol.*, *267*(3), 160–172.

Binley, A., S. S. Hubbard, J. A. Huisman, A. Revil, D. A. Robinson, K. Singha, and L. D. Slater (2015), The emergence of hydrogeophysics for improved understanding of subsurface processes over multiple scales, *Water Resour. Res.*, *51*, 3837–3866, doi:10.1002/2015WR017016.

Briggs, M. A., F. D. Day-Lewis, J. B. T. Ong, G. P. Curtis, and J. W. Lane (2013), Simultaneous estimation of local-scale and flow path-scale dual-domain mass transfer parameters using geoelectrical monitoring, *Water Resour. Res.*, *49*, 5615–5630, doi:10.1002/wrcr.20397.

Campbell, R., C. Bower, and L. Richards (1948), Change of electrical conductivity with temperature and the relation of osmotic pressure to electrical conductivity and ion concentration in soil extracts, *Soil Sci. Soc. Am. Proc.*, *13*, 66–69.

Carrigan, C. R., et al. (2013), Electrical resistance tomographic monitoring of CO2 movement in deep geologic reservoirs, *Int. J. Greenhouse Gas Control*, *18*, 401–408, doi:10.1016/j.ijggc.2013.04.016.

Caterina, D., J. Beaujean, T. Robert, and F. Nguyen (2013), A comparison study of different image appraisal tools for electrical resistivity tomography, *Near Surf. Geophys.*, *11*, 639–657, doi:10.3997/1873-0604.2013022.

Caterina, D., T. Hermans, and F. Nguyen (2014), Case studies of incorporation of prior information in electrical resistivity tomography: Comparison of different approaches, *Near Surf. Geophys.*, *12*, 451–465, doi:10.3997/1873-0604.2013070.

Chen, X., H. Murakami, M. S. Hahn, G. E. Hammond, M. L. Rockhold, J. M. Zachara, and Y. Rubin (2012), Three-dimensional Bayesian geostatistical aquifer characterization at the Hanford 300 Area using tracer test data, *Water Resour. Res.*, *48*, W06501, doi:10.1029/2011WR010675.

Chrétien, M., J. F. Lataste, R. Fabre, and A. Denis (2014), Electrical resistivity tomography to understand clay behavior during seasonal water content variations, *Eng. Geol.*, *169*, 112–123, doi:10.1016/j.enggeo.2013.11.019.

Christensen, N.K., S. Christensen, and T.P.A. Ferre (2016), Testing alternative uses of electromagnetic data to reduce the prediction error of groundwater models, *Hydrol. Earth Syst. Sci.*, *20*(5), 1925–1946, doi:10.5194/hess-20-1925-2016.

Day-Lewis, F. D., K. Singha, and A. Binley (2005), Applying petrophysical models to radar travel time and electrical resistivity tomograms: Resolution-dependent limitations, *J. Geophys. Res.*, *110*, B08206, doi:10.1029/2004JB003569.

Day-Lewis, F. D., Y. Chen, and K. Singha (2007), Moment inference from tomograms, *Geophys. Res. Lett.*, *34*, L22404, doi:10.1029/2007GL031621.

Doetsch, J., N. Linde, and A. Binley (2010), Structural joint inversion of time-lapse crosshole ERT and GPR traveltime data, *Geophys. Res. Lett.*, *37*, L24404, doi:10.1029/2010GL045482.

Doetsch, J., N. Linde, T. Vogt, A. Binley, and A. G. Green (2012), Imaging and quantifying salt-tracer transport in a riparian groundwater system by means of 3D ERT monitoring, *Geophysics*, *77*(5), B207–B218, doi:10.1190/geo2012-0046.1.

Fiandaca, G., J. Doetsch, G. Vignoli, and E. Auken (2015), Generalized focusing of time-lapse changes with applications to direct current and time-domain induced polarization inversions, *Geophys. J. Int.*, *203*(2), 1101–1112.

Flores Orozco, A., A. Kemna, and E. Zimmermann (2012), Data error quantification in spectral induced polarization imaging, *Geophysics*, *77*(3), E227–E237, doi:10.1190/GEO2010-0194.1.

Hansen, T. M., K. S. Cordua, B. H. Jacobsen, and K. Mosegaard (2014), Accounting for imperfect forward modeling in geophysical inverse problems — Exemplified for crosshole tomography, *Geophysics*, *79*(3), H1–H21, doi:10.1190/geo2013-0215.1.

Hermans, T., A. Vandenbohede, L. Lebbe, and F. Nguyen (2012), A shallow geothermal experiment in a sandy aquifer monitored using electric resistivity tomography, *Geophysics*, *77*(1), B11–B21, doi:10.1190/geo2011-0199.1.

Hermans, T., F. Nguyen, T. Robert, and A. Revil (2014), Geophysical methods for monitoring temperature changes in shallow low enthalpy geothermal systems, *Energies*, *7*(8), 5083–5118, doi:10.3390/en7085083.

Hermans, T., S. Wildemeersch, P. Jamin, P. Orban, S. Brouyère, A. Dassargues, and F. Nguyen (2015), Quantitative temperature monitoring of a heat tracing experiment using cross-borehole ERT, *Geothermics*, *53*, 14–26, doi:10.1016/j.geothermics.2014.03.013.

Hermans, T., A. Kemna, and F. Nguyen (2016), Covariance-constrained difference inversion of time-lapse electrical resistivity tomography data, *Geophysics*, *81*(5), E311–E322.

Hinnell, A. C., T. P. Ferré, J. A. Vrugt, J. A. Huisman, S. Moysey, J. Rings, and M. B. Kowalsky (2010), Improved extraction of hydrologic information from geophysical data through coupled hydrogeophysical inversion, *Water Resour. Res.*, *46*, W00D40, doi:10.1029/2008WR007060.

Irving, J., and K. Singha (2010), Stochastic inversion of tracer test and electrical geophysical data to estimate hydraulic conductivities, *Water Resour. Res.*, *46*, W11514, doi:10.1029/2009WR008340.

Johnson, T. C., L. D. Slater, D. Ntarlagiannis, F. D. Day-Lewis, and M. Elwaseif (2012), Monitoring groundwater-surface water interaction using time-series and time-frequency analysis of transient three-dimensional electrical resistivity changes, *Water Resour. Res.*, *48*, W07506, doi:10.1029/2012WR011893.

Johnson, T. C., R. J. Versteeg, F. D. Day-Lewis, W. Major, and J. W. Lane (2015), Time-lapse electrical geophysical monitoring of amendment-based biostimulation, *Ground Water*, *53*(6), 920–932, doi:10.1111/gwat.12291.
Karaoulis, M., J. H. Kim, and P. Tsourlos (2011), 4D active time constrained resistivity inversion, *J. Appl. Geophys.*, *73*, 25–34.
Kemna, A., B. Kulessa, and H. Vereecken (2002), Imaging and characterisation of subsurface solute transport using electrical resistivity tomography (ERT) and equivalent transport models, *J. Hydrol.*, *267*(3-4), 125–146.
Kim, J. H., M. J. Yi, S. G. Park, and J. G. Kim (2009), 4-D inversion of DC resistivity monitoring data acquired over a dynamically changing earth model, *J. Appl. Geophys.*, *68*(4), 522–532.
Koestel, J., A. Kemna, M. Javaux, A. Binley, and H. Vereecken (2008), Quantitative imaging of solute transport in an unsaturated and undisturbed soil monolith with 3-D ERT and TDR, *Water Resour. Res.*, *44*, W12411, doi:10.1029/2007WR006755.
Krzanowski, W. J. (2000), *Principles of Multivariate Analysis: A User's Perspective, Oxford Stat.* Ser. 22, revised ed., Oxford Univ. Press, N. Y.
LaBrecque, D. J., M. Miletto, W. Daily, A. Ramirez, and E. Owen (1996), The effects of noise on Occam's inversion of resistivity tomography data, *Geophysics*, *61*(2), 538–548.
Laloy, E., N. Linde, and J. A. Vrugt (2012), Mass conservative three-dimensional water tracer distribution from Markov chain Monte Carlo inversion of time-lapse ground-penetrating radar data, *Water Resour. Res.*, *48*, W07510, doi:10.1029/2011WR011238.
Linde, N., P. Renard, T. Mukerji, and J. Caers (2015), Geological realism in hydrogeological and geophysical inverse modeling: A review, *Adv. Water Resour.*, *86*, 86–101, doi:10.1016/j.advwatres.2015.09.019.
Lochbühler, T., G. Pirot, J. Straubhaar, and N. Linde (2014), Conditioning of multiple-point statistics facies simulations to tomographic images, *Math. Geosci.*, *46*(5), 625–645, doi:10.1007/s11004-013-9484-z.
Masy, T., D. Caterina, O. Tromme, B. Lavigne, P. Thonart, S. Hiligsmann, and F. Nguyen (2016), Electrical resistivity tomography to monitor enhanced biodegradation of hydrocarbons with Rhodococcus erythropolis T902.1 at a pilot scale, *J. Contam. Hydrol.*, *184*, 1–13, doi:10.1016/j.jconhyd.2015.11.001.
Moysey, S., K. Singha, and R. Knight (2005), A framework for inferring field-scale rock physics relationships through numerical simulation, *Geophys. Res. Lett.*, *32*, L08304, doi:10.1029/2004GL022152.
Müller, K., J. Vanderborght, A. Englert, A. Kemna, J. A. Huisman, J. Rings, and H. Vereecken (2010), Imaging and characterization of solute transport during two tracer tests in a shallow aquifer using electrical resistivity tomography and multilevel groundwater samplers, *Water Resour. Res.*, *46*, W03502, doi:10.1029/2008WR007595.
Murakami, H., X. Chen, M. S. Hahn, Y. Liu, M. L. Rockhold, V. R. Vermeul, J. M. Zachara, and Y. Rubin (2010), Bayesian approach for three-dimensional aquifer characterization at the Hanford 300 Area, *Hydrol. Earth Syst. Sci.*, *14*(10), 1989–2001, doi:10.5194/hess-14-1989-2010.
Nguyen, F., A. Kemna, T. Robert, and T. Hermans (2016), Data-driven selection of the minimum-gradient support parameter in time-lapse focused electric imaging, *Geophysics*, *81*(1), A1–A5, doi:10.1190/GEO2015-0226.1.
Oware, E. K., and S. M. J. Moysey (2014), Geophysical evaluation of solute plume spatial moments using an adaptive POD algorithm for electrical resistivity imaging, *J. Hydrol.*, *517*, 471–480, doi:10.1016/j.jhydrol.2014.05.054.
Oware, E. K., S. M. J. Moysey, and T. Khan (2013), Physically based regularization of hydrogeophysical inverse problems for improved imaging of process-driven systems, *Water Resour. Res.*, *49*, 6238–6247, doi:10.1002/wrcr.20462.
Pidlisecky, A., K. Singha, and F. D. Day-Lewis (2011), A distribution-based parametrization for improved tomographic imaging of solute plumes, *Geophys. J. Int.*, *187*(1), 214–224, doi:10.1111/j.1365-246X.2011.05131.x.
Robert, T., D. Caterina, J. Deceuster, O. Kaufmann, and F. Nguyen (2012), A salt tracer test monitored with surface ERT to detect preferential flow and transport paths in fractured/karstified limestones, *Geophysics*, *77*, B55–B67.
Rubin, Y., and S. Hubbard (2005), *Hydrogeophysics*, Water Sci. and Technol. Libr., Springer, Dordrecht, Netherlands.
Rubin, Y., X. Chen, H. Murakami, and M. Hahn (2010), A Bayesian approach for inverse modeling, data assimilation, and conditional simulation of spatial random fields, *Water Resour. Res.*, *46*, W10523, doi:10.1029/2009WR008799.
Satija, A., and J. Caers (2015), Direct forecasting of subsurface flow response from non-linear dynamic data by linear least-squares in canonical functional principal component space, *Adv. Water Resour.*, *77*, 69–81, doi:10.1016/j.advwatres.2015.01.002.
Scheidt, C., P. Renard, and J. Caers (2015), Prediction-focused subsurface modeling: Investigating the need for accuracy in flow-based inverse modeling, *Math. Geosci.*, *47*(2), 173–191, doi:10.1007/s11004-014-9521-6.
Singha, K., and S. M. Gorelick (2005), Saline tracer visualized with three-dimensional electrical resistivity tomography: Field-scale spatial moment analysis, *Water Resour. Res.*, *41*, W05023, doi:10.1029/2004WR003460.
Singha, K., and S. Moysey (2006), Accounting for spatially variable resolution in electrical resistivity tomography through field-scale rock-physics relations, *Geophysics*, *71*(4), A25–A28, doi:10.1190/1.2209753.
Singha, K., F. D. Day-Lewis, T. Johnson, and L. Slater (2015), Advances in interpretation of subsurface processes with time-lapse electrical imagin, *Hydrol. Processes*, *29*(6), 1549–1576.
Strebelle, S. (2002), Conditional simulation of complex geological structures using multiple-point statistics, *Math. Geol.*, *34*(1), 1–21.
Tarantola, A. (2005), *Inverse Problem Theory and Methods for Model Parameter Estimation*, Soc. for Ind. and Appl. Math., Philadelphia, Penn.
Therrien, R., R. McLaren, E. Sudicky, and S. Panday (2010), *HydroGeoSphere: A Three-Dimensional Numerical Model Describing Fully-Integrated Subsurface and Surface Flow and Solute Transport*, Groundwater Simul. Group, Waterloo, Ont., Canada.
Tonkin, M. J., and J. Doherty (2005), A hybrid regularized inversion methodology for highly parameterized environmental models, *Water Resour. Res.*, *41*, W10412, doi:10.1029/2005WR003995.
Truex, M. J., T. C. Johnson, C. E. Strickland, J. E. Peterson, and S. S. Hubbard (2013), Monitoring Vadose Zone Desiccation with Geophysical Methods, *Vadose Zone J.*, *12*(2), 14, doi:10.2136/vzj2012.0147.
Vanderborght, J., A. Kemna, H. Hardelauf, and H. Vereecken (2005), Potential of electrical resistivity tomography to infer aquifer transport characteristics from tracer studies: A synthetic case study, *Water Resour. Res.*, *41*, W06013, doi:10.1029/2004WR003774.
Vereecken, H., A. Binley, G. Cassiani, A. Revil, and K. Titov (2007), *Applied Hydrogeophysics, NATO Sci. Ser. IV. Earth Environ. Sci.*, Springer, Dordrecht, Netherlands.
Wallin, E. L., T. C. Johnson, W. J. Greenwood, and J. M. Zachara (2013), Imaging high stage river-water intrusion into a contaminated aquifer along a major river corridor using 2-D time-lapse surface electrical resistivity tomography, *Water Resour. Res.*, *49*, 1693–1708, doi:10.1002/wrcr.20119.
Zhou, B., and S. A. Greenhalgh (2000), Cross-hole resistivity tomography using different electrode configurations, *Geophys. Prospect.*, *48*(5), 887–912.

Erratum

In the previously published version of this article, the first author's first name and surname were erroneously switched. This may be considered the authoritative version.